LBL-21084 c.2

Lawrence Berkeley Laboratory

UNIVERSITY OF CALIFORNIA

RECEIVED
LAWRENCE
BERKELEY LABORATORY
1986
LIBRARY AND

Physics Division

SEARCH FOR RIGHT-HANDED CURRENTS IN MUON DECAY

A.E. Jodidio
(Ph.D. Thesis)

January 1986

TWO-WEEK LOAN COPY
This is a Library Circulating Copy
which may be borrowed for two weeks.

LBL-21084 c.2

Prepared for the U.S. Department of Energy under Contract DE-AC03-76SF00098

DISCLAIMER

This document was prepared as an account of work sponsored by the United States Government. While this document is believed to contain correct information, neither the United States Government nor any agency thereof, nor the Regents of the University of California, nor any of their employees, makes any warranty, express or implied, or assumes any legal responsibility for the accuracy, completeness, or usefulness of any information, apparatus, product, or process disclosed, or represents that its use would not infringe privately owned rights. Reference herein to any specific commercial product, process, or service by its trade name, trademark, manufacturer, or otherwise, does not necessarily constitute or imply its endorsement, recommendation, or favoring by the United States Government or any agency thereof, or the Regents of the University of California. The views and opinions of authors expressed herein do not necessarily state or reflect those of the United States Government or any agency thereof or the Regents of the University of California.

LBL-21084

Search for Right-Handed Currents in Muon Decay

Alexander Ezra Jodidio

Ph.D. Thesis

January 1986

Lawrence Berkeley Laboratory

University of California

Berkeley, CA 94720

This work was supported by the Director, Office of Energy Research, Office of High Energy and Nuclear Physics, Division of High Energy Physics of the U. S. Department of Energy under contract #DE-AC03-76SF00098.

Search for Right-Handed Currents in Muon Decay

Alexander Ezra Jodidio

Abstract

Limits are reported on charged right-handed currents, based on precise measurement of the endpoint e^+ spectrum in μ^+ decay. Highly polarized μ^+ from the TRIUMF "surface" muon beam were stopped in high purity metal foils and liquid He targets selected to minimize depolarization effects. Decay e^+ emitted within 160 mrad of the beam direction were momentum-analyzed to 0.15%. Muons were stopped within either a spin-precessing transverse field (70-G or 110-G) or a spin-holding longitudinal field (0.3-T or 1.1-T). Data collected with the spin-precessing field were used for the momentum calibration of the spectrometer. The spin-held data were used to measure the relative e^+ rate at the endpoint. An extrapolation was made to extract the endpoint rate opposite to the μ^+ spin. In terms of the standard muon decay parameters this rate is given by $(1-\xi P_\mu \delta/\rho)$ where P_μ is muon polarization. The result for $\xi P_\mu \delta/\rho$ was consistent with the V-A prediction of 1. It is quoted as a 90% confidence lower limit $\xi P_\mu \delta/\rho > 0.9975$ since we are unable to correct for all possible sources of muon depolarization. For the model with manifest left-right symmetry and massless neutrinos the result implies 90%

confidence limits $m(W_2)>432$ GeV/c^2 and $-0.050<\zeta<0.035$, where W_2 is the predominantly right-handed boson and ζ is the left-right mixing angle. With the assumption of no left-right mixing an equivalent 90% confidence upper limit of 0.025 is obtained on the absolute value of the ratio of a possible V+A amplitude to the dominant V-A amplitude in muon and pion decays. Limits are also deduced on the $\nu_{\mu L}$ mass and helicity in π^+ decay, non-(V-A) couplings in helicity projection form, the mass scale of composite leptons, and the branching ratio for $\mu \to e+f$ where f (familon) is the neutral massless Nambu-Goldstone boson associated with flavor symmetry breaking.

Table of Contents

Acknowledgements iv

I. Introduction 1

II. Muon Decay Spectrum 6

III. Experimental Setup 13

A. Overview 13

B. The Beamline 16

C. Muon Deceleration and Thermalization . . 21

D. The Muon Polarimeter 24

E. The Trigger 27

IV. Event Reconstruction and Selection 29

V. Data Analysis 33

A. The Fitting Procedure 34

B. Computation of $\cos\theta_{av}$ 39

C. Summary of the Analysis Method . . . 44

D. Data Fitting Results 46

VI. Corrections 53

A. Correction due to Multiple Scattering and Finite Chamber Resolution 55

B. Correction due to Use of Data-Averaged $\cos\theta_\mu \cos\theta_e$ 62

C. Muon Depolarization in Scattering with Unpolarized Electrons 64

VII. Systematic Errors 67

A. x=1 Calibration 67

B. Momentum Acceptance 70

C. Momentum Dispersion 72

D. Reconstruction of $\cos\theta_\mu$ and $\cos\theta_e$ 73

E. Extra Muons 75

VIII. Discussion and Conclusions 78

A. Limit on $\xi P_\mu \delta/\rho$ 78

B. Limits on Right-Handed Currents with Massless Neutrinos 79

C. Limits on $m(\nu_{\mu L})$ and $\nu_{\mu L}$ Helicity in π^+ Decay 80

D. Restriction on the Lorentz Structure of Leptonic Charged Weak Interactions . . 80

E. Limits on Composite Leptons 83

F. Limits on Familons 85

G. Limits on $m(W_2)$ with $m(\nu_{\mu R})\neq 0$ 86

H. Concluding Remarks 89

Appendix A. Stopping Targets 90

Appendix B. Table of Data Fitting Results . . 94

Appendix C. Computation of Limits on $m(W_2)$ with $m(\nu_{\mu R})\neq 0$ 97

References 103

Acknowledgements

This thesis is based on the results from experiment 185 performed at the TRIUMF meson facility by a collaboration from LBL/University of California at Berkeley, Northwestern University, and TRIUMF. The success of the experiment was made possible by the efforts of all collaborators: Brian Balke, John Carr, George Gidal, Bruno Gobbi, Chris Oram, Kirk Shinsky (deceased), Herb Steiner, David Stoker, Mark Strovink (spokesman), Bob Tripp, and myself. The technical assistance of C. Covey, R. Fuzesy, F. Goozen, P. Harding, M. Morrison, and P. Robrish at LBL and the support of the TRIUMF staff contributed to the success of the experiment.

I would like to expess my sincere appreciation to my advisor, Professor H.M. Steiner, for his strong support throughout my work on this experiment.

I wish to thank the members of my thesis committee, professors H.M. Steiner, M. Strovink and S. Kaplan for making many helpful comments on this thesis. Thanks are also due to my fellow graduate student Brian Balke for many helpful suggestions on chapters VI and VII.

I would also like to thank professor Bruno Gobbi of Northwestern University for his hospitality and his assistance during the analysis of the data at Evanston in the summer of 1983.

I cannot say enough to express my gratitude to my wife, Anna Rozenshtein, for her encouragement and moral support. Without her this thesis may not have been completed.

I, and I am sure all other members of the collaboration, have sorely missed the presence of Kirk Shinsky, who was tragically stricken by cancer and passed away on September 6, 1983. We deeply regret that he did not see the final results from this experiment, to which he made such a strong contribution.

The research reported here was supported in part by the U.S. Department of Energy through Contracts No. DE-AC03-76SF00098 and AC02-ER02289.

I. INTRODUCTION

In the widely accepted Glashow-Weinberg-Salam (GWS) $SU(2)_L \times U(1)$ model of weak and electromagnetic interactions[1] the V-A structure of weak interaction has been put in a priori to obtain agreement with experiments. Although the model agrees with all experimental results up to presently available energies, the experimental precision has not been sufficient to rule out relatively large deviations from the V-A structure.[2] We have made a sensitive search for such deviations by measuring the muon decay spectrum near the end-point. Our result is particularly suited for setting stringent limits on charged right-handed, i.e. V+A, currents, and for constraining parameters in the left-right symmetric models.

The left-right symmetric (LRS) models,[3] based on the gauge group $SU(2)_R \times SU(2)_L \times U(1)$, have been intensively studied as extensions of the standard GWS model. Such models have a great aesthetic appeal because the Lagrangian has a L-R symmetry and parity conservation is restored at moderate energies. In such models the V-A nature of weak interaction at low energies is due to the spontaneous symmetry breaking mechanism, as a result of which the predominantly right-handed gauge boson W_2 acquires a heavier mass than the predominantly left-handed boson W_1.[4] The mass-squared ratio of physical bosons W_1 and W_2 will be denoted by $\varepsilon = m^2(W_1)/m^2(W_2)$. The mass eigenstates W_1 and W_2 are related to W_L and W_R by a mixing angle ζ, $W_1 = W_L \cos\zeta - W_R \sin\zeta$, $W_2 = W_L \sin\zeta + W_R \cos\zeta$.

Let us review the existing limits on charged right-handed

currents. The limits that can be obtained from leptonic and semi-leptonic weak processes depend on the masses of the associated right-handed neutrinos. If neutrinos are Dirac fermions, ν_L and ν_R must necessarily have the same mass, since they are different helicity states of the same particle. In this case the predominantly right-handed boson W_2 participates in low-energy processes. However, in some attractive theories neutrinos are Majorana particles.[5] Since there can be both Majorana and Dirac mass terms in the neutrino mass matrix, the physical neutrinos ν_1 and ν_2 may have different masses. In most models the predominantly left-handed neutrino ν_1 is predicted to be very light, $m(\nu_1) \sim m_e^2/m(W_2)$, while the predominantly right-handed neutrino ν_2 is very heavy, $m(\nu_2) \sim m(W_2)$, and therefore cannot be produced in low energy experiments. The physical neutrinos ν_1 and ν_2 are related to ν_L and ν_R by a mixing angle δ, expected to be of the order of $m_e/m(W_2)$. Ignoring the very small neutrino mixing angle, purely leptonic processes, requiring production of at least one ν_2, do not set limits on right-handed currents in such theories. Semi-leptonic processes such as νN and $\bar{\nu} N$ scattering, which do not require a production of ν_2, can still set a limit on the mixing angle ζ.

Hadronic weak processes set limits on right-handed currents independently of ν_R masses. In a class of models, called 'manifestly' L-R symmetric, the left-handed and right-handed Kobayashi-Maskawa quark mixing angles are assumed to be identical, and CP invariance is assumed to hold. In these models the K_L-K_S mass difference requires $m(W_2) > 1.6$ TeV,[6] and current algebra analysis of

$\Delta S=1$ decays yields $\zeta \leq 0.004$, $m(W_2)>300$ GeV for $\zeta=0$.[7] If left-handed and right-handed mixing angles are not identical (which is a very unnatural and unaesthetic assumption), hadronic processes are consistent with $m(W_2)\sim 300$ GeV.[8]

Another strong limit on the mixing angle ζ, $\zeta<0.005$, has been obtained in a model-dependent analysis of semileptonic weak processes, assuming again manifest L-R symmetry.[9]

The contours corresponding to 90% confidence limits[10] on ε and ζ from the experiments in β decay, μ decay and νN, $\bar{\nu}N$ scattering, are shown in Fig. I.1. The allowed regions contain the origin $\varepsilon=\zeta=0$, which is the V-A limit. Manifest L-R symmetry has been assumed. The contours from μ and β decay experiments have been plotted with the assumption that the right-handed neutrinos are sufficiently light not to affect the kinematics. The bold ellipse in Fig. I.1 is the combined result from the analysis of muon decay spectrum at the end-point, opposite the μ^+ spin, presented in this thesis, and from the μSR analysis published previously.[11,12] The other muon-decay contours are derived from the measurement of the polarization parameter ξP_μ (dotted curve, Ref. 13) and the Michel parameter ρ (solid curve, Ref. 14). Nuclear β decay contours are derived from the Gamow-Teller β polarization (dot-dashed curve, Ref. 15); the comparison of Gamow-Teller and Fermi β polarizations (long-dashed curves, Ref. 16); and the ^{19}Ne asymmetry A(0) and ft ratio, with the assumption of conserved vector current (short-dashed curves, Ref. 17). The limits from the y distributions in νN, $\bar{\nu}N$ scattering (double lines, Ref. 18) are valid irrespective of ν_R mass.

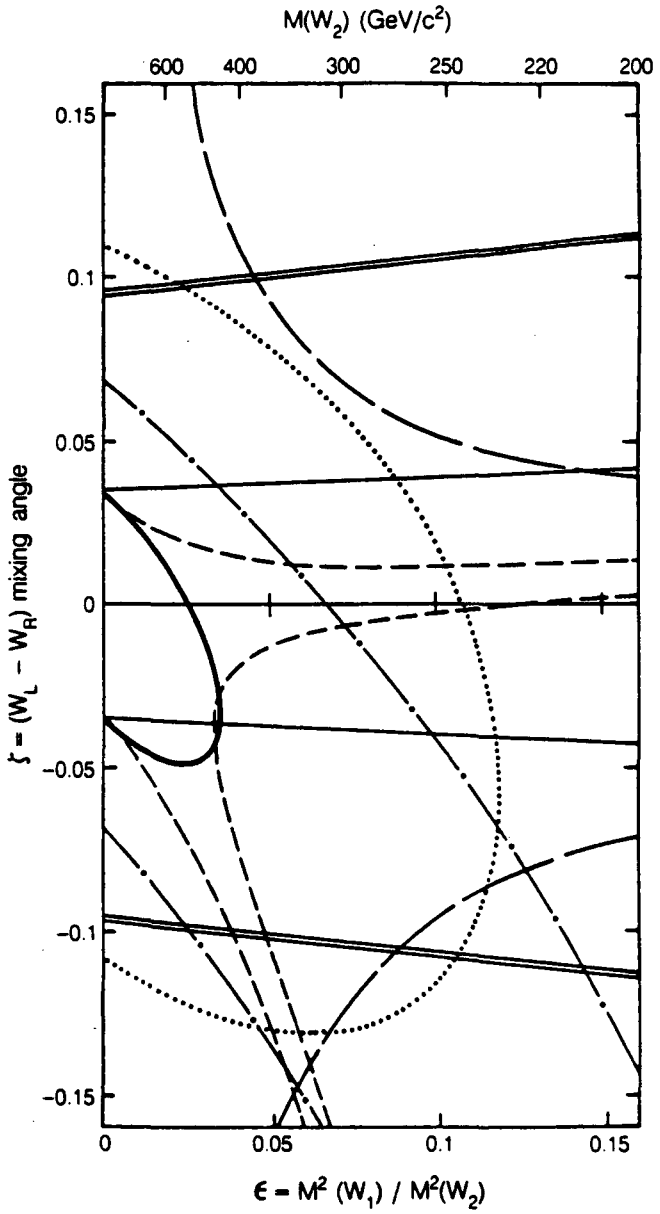

FIG. I.1. Experimental 90%-confidence limits on the mass-squared ratio ε and mixing angle ζ for the gauge bosons W_1 and W_2. The allowed regions are those which include $\varepsilon=\zeta=0$. The sources of the limits are described in the text.

The rest of this thesis is organized as follows. In section II we discuss the properties of the muon decay spectrum and present the basic idea in the data analysis. The beamline and experimental apparatus are discussed in section III. Event reconstruction and selection are considered in section IV. Data analysis and data fitting results are presented in section V. Corrections and systematic errors are discussed in sections VI and VII. The conclusions from the experimental result are drawn in section VIII.

II. MUON DECAY SPECTRUM

In the discussion of the muon decay spectrum we will assume that neutrinos are sufficiently light not to affect the kinematics. We will return to the question of massive neutrinos in section VIII.

The muon differential decay rate for an interaction mediated by a heavy vector boson W differs from the decay rate computed with the corresponding four-fermion contact interaction Hamiltonian by terms[19] of order $(m_\mu/M_W)^2$. These terms are $\sim 10^{-6}$ for $M_W \approx 80$ GeV/c^2 and are negligible at the present level of experimental precision. Consequently we will use the expression for the muon decay spectrum computed for a four-fermion contact interaction.

If radiative corrections are ignored, the muon differential decay rate,[20] integrated over e^+ spin directions, is given by

$$\frac{d^2\Gamma}{x^2\, dx d(\cos\theta)} \sim [(3-2x)+(\tfrac{4}{3}\rho-1)(4x-3)+12\,\frac{m_e}{m_\mu}\,\frac{x-1}{x}\,\eta] - [(2x-1)+(\tfrac{4}{3}\delta-1)(4x-3)]\xi P_\mu \cos\theta \quad . \tag{2.1}$$

Here x is the standard reduced energy variable $x=E_e/E_{max}$, where $E_{max}=(m_e{}^2+m_\mu{}^2)/(2m_\mu)=52.83$ MeV is the maximum energy; m_e and m_μ are the particle masses. The effects of finite positron mass are neglected in the above formula but not in the analysis. $\pi-\theta$ is the angle between positron momentum and muon polarization vector P_μ in the μ^+ rest frame. The four muon decay parameters ρ, η, ξ, δ have been previously measured, and their world average values[21] prior to our experiment are given in Table II.1. The values these parameters take in the L-R symmetric model are also listed in Table II.1 to

TABLE II.1. Values of the muon decay parameters ρ, η, ξ, δ in the V-A model and the manifestly left-right symmetric (LRS) model with massless neutrinos. Their world-average experimental values[21] prior to our experiment are also listed. The values in the LRS model are given to the lowest order in the mass-squared ratio ε and mixing angle ζ for the gauge bosons W_1 and W_2.

Decay Parameter	V-A Value	Value in in the LRS model	Experimental Value
ρ	$\frac{3}{4}$	$\frac{3}{4}(1-2\zeta^2)$	0.7517 ± 0.0026
η	0	0	0.06 ± 0.15
ξ	1	$1-2\varepsilon^2-2\zeta^2$	ξP_μ: 0.972 ± 0.014
P_μ^*	1	$1-2(\varepsilon+\zeta)^2$	
δ	$\frac{3}{4}$	$\frac{3}{4}$	0.7551 ± 0.0085

* P_μ is the muon longitudinal polarization from π^+ decay at rest.

lowest order in ε and ζ. The V-A values correspond to $\varepsilon=\zeta=0$.

The first order electromagnetic corrections to the muon decay spectrum are rather large (several %) since their magnitude is not of order α (fine-structure constant) but $\alpha\ln(m_\mu{}^2/m_e{}^2)$. The radiative corrections can be computed accurately with the (four-fermion contact) Fermi interaction Hamiltonian,[22] since the heavy intermediate vector bosons contribute negligible additional terms[23] of order $\alpha(m_\mu/m_W)^2$. The first-order corrections have been computed for the general Fermi interaction,[24] and this general expression was used in Monte-Carlo simulations to verify the accuracy of the analysis method. For the analysis itself only the V-A corrections were needed.

The radiatively corrected muon decay spectrum for a pure V-A interaction is shown in Fig. II.1 for $\cos\theta$ equal to -1, 0 and +1. The spectrum for unpolarized muons corresponds to the $\cos\theta=0$ curve, whose sharp edge at x=1 played an important role in the momentum calibration of our spectrometer. For $\cos\theta=1$ the V-A rate vanishes at the end-point as expected from angular momentum conservation.

The V+A spectrum at $\cos\theta$ is equivalent to the V-A spectrum at $(-\cos\theta)$. The region of greatest experimental sensitivity to an admixture of right-handed currents is therefore near x and $\cos\theta$ equal to 1. In that region of phase space the V-A rate vanishes, while the V+A rate is maximum. Our experiment was designed to measure the positron spectrum for $x>.85$ and $\cos\theta>.95$.

The data analysis was based on the following property of the muon decay spectrum: if the weak interaction is predominantly V-A, with a

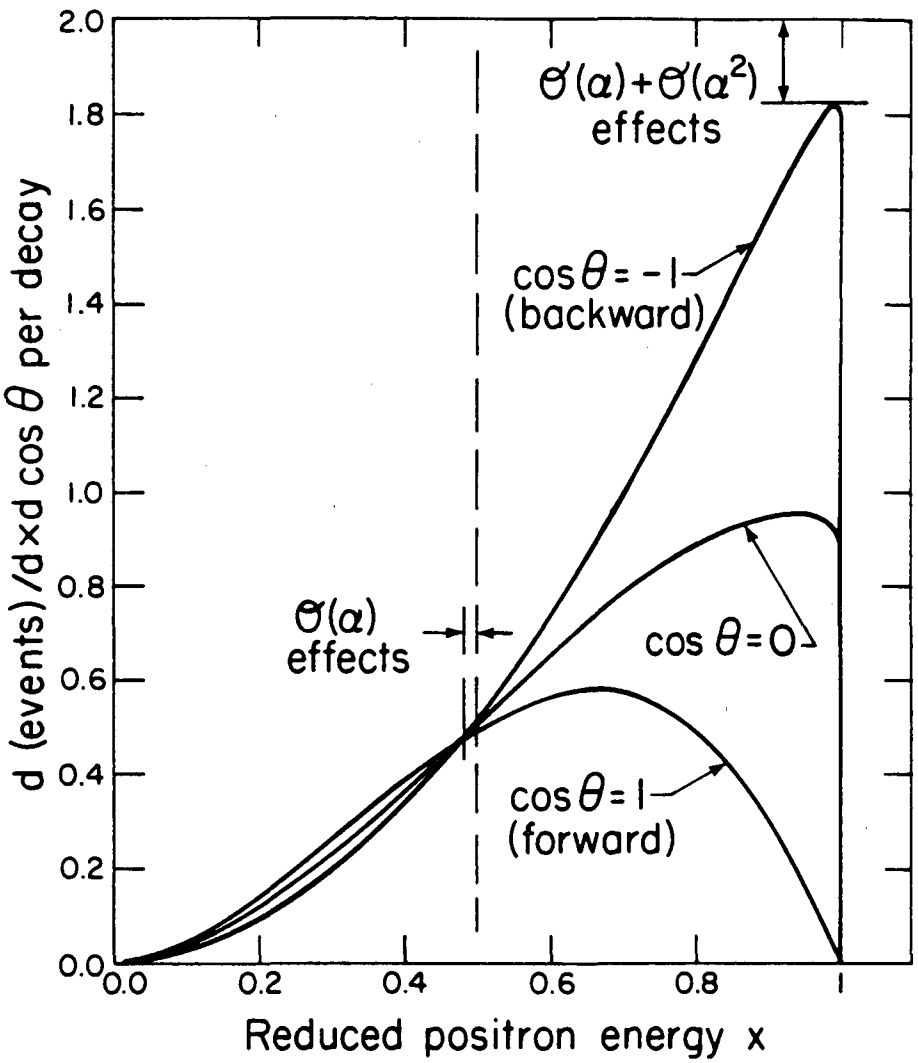

XBL 8512-11756

FIG. II.1. The V-A radiatively corrected muon decay spectrum plotted for cos θ=+1, 0 and -1. The effects of radiative corrections are also indicated.

small admixture of V+A, scalar, tensor or pseudoscalar currents, then the positron spectrum near the endpoint, for $\cos\theta \approx 1$, can be expressed as a sum of two pure V-A spectra: one with $P_\mu = \cos\theta = 1$ and another with $P_\mu \cos\theta = 0$. An intuitive explanation is that near the end-point a positron spectrum at a particular value of $\cos\theta$ is given essentially by a sum of a linear function characteristic of the $P_\mu \cos\theta = 1$ V-A spectrum, which vanishes at $x=1$, and a step function, represented by the unpolarized, $P_\mu \cos\theta = 0$, V-A spectrum. The relative size of the step or the rate at the endpoint is $1 - \xi P_\mu \cos\theta \delta/\rho$. Measurement of the rate as a function of $\cos\theta$ allows us to extract $\xi P_\mu \delta/\rho$.

In order to simplify the algebra it will be convenient to use

$$\tilde{\rho} = 1 - \frac{4}{3}\rho$$
$$\tilde{\delta} = 1 - \frac{4}{3}\delta$$

with $\tilde{\rho} = \tilde{\delta} = 0$ for a pure V-A interaction. The decay spectra will be denoted by

$S(x, P_\mu \cos\theta)$ - spectrum for an arbitrary weak coupling (i.e. arbitrary values of ξ, ρ, δ) and a particular value of $P_\mu \cos\theta$

$S_{V-A}(x,1)$ - V-A spectrum at $P_\mu \cos\theta = 1$ with the same normalization as $S(x, P_\mu \cos\theta)$

$S_{V-A}(x,0)$ - V-A spectrum at $P_\mu \cos\theta = 0$ with the same normalization as $S(x, P_\mu \cos\theta)$.

Let us ignore for the moment the radiative corrections. Since near the endpoint the η term in (2.1) is negligible and can be ignored, there is an exact relationship

$$S(x, P_\mu \cos\theta) = q(\theta) S_{V-A}(x,1) + r(\theta) S_{V-A}(x,0) \qquad (2.2)$$

where

$$q(\theta)=\xi P_\mu \cos\theta - \frac{1}{2}\tilde{\delta}\xi P_\mu \cos\theta + \frac{1}{2}\tilde{\rho} \ . \tag{2.3}$$

and $r(\theta)$ is the relative rate at the end-point

$$r(\theta)=(1-\xi P_\mu \cos\theta)+\tilde{\delta}\xi P_\mu \cos\theta - \tilde{\rho} \tag{2.4}$$

Equations (2.3) and (2.4) can be rewritten in a simpler form using the smallness of $\tilde{\rho}$ and $\tilde{\delta}$ (~.01), and the fact that $\xi P_\mu \cos\theta$ is approximately 1. To first order in $\tilde{\rho}$, $\tilde{\delta}$, $r(\theta)$ and $q(\theta)$ take the simple forms

$$r(\theta)=1-\xi P_\mu \frac{\delta}{\rho}\cos\theta \ . \tag{2.5}$$

and

$$q(\theta)=1-r(\theta)=\xi P_\mu \frac{\delta}{\rho}\cos\theta \ . \tag{2.6}$$

When radiative corrections are included, the exact relation (2.2) becomes only an approximation, and if the data were fitted according to (2.2), with $q(\theta)=1-r(\theta)$, then $r(\theta)$ would only approximately correspond to (2.5). The high precision of this measurement has required a detailed study of the effect of the radiative corrections. For the fitting procedure to be described in section V, it was checked, that for a spectrum given by a combination of only V+A and V-A effective couplings, the radiative corrections had a very small effect on the value found for $r(\theta)$. Hence, within the experimental errors, $\xi P_\mu \delta/\rho$ could be extracted from $r(\theta)$ as in (2.5) without introducing an additional systematic error. If our result is to be used for setting limits on the presence of other effective weak couplings, it must be verified that when all couplings are taken into account, the radiative corrections do not introduce an additional

systematic error.

The highly polarized muons in our experiment were obtained by means of a "surface" muon beam,[25] derived from pions decaying at rest near a surface of the production target. Right-handed currents would reduce muon polarization in pion decay to $P_\mu=1-2(\varepsilon+\zeta)^2$ (assuming manifest left-right symmetry). When this effect is included, our final result is given in terms of ε and ζ by

$$\xi P_\mu \delta/\rho=1-2(2\varepsilon^2+2\varepsilon\zeta+\zeta^2) \ .$$

Since we are unable to correct for all possible sources of muon depolarization, our result can be interpreted only as a lower limit on $\xi P_\mu \delta/\rho$.

III. EXPERIMENTAL METHOD

III.A. Overview

The experiment was made possible by the nearly complete polarization of the "surface" muon beam, derived from pions decaying at rest near the surface of the production target. The "surface" muons were transported in vacuum by the M13 beamline at the TRIUMF cyclotron to a stopping target in the muon polarimeter, shown schematically in Fig. III.1. High-purity metal foils (Ag, Al, Au, Cu) and liquid He were selected as stopping targets, since in these materials muonium (μ^+-e^- atom) formation, leading to muon depolarization, is strongly suppressed.

The target region was immersed either in a strong longitudinal 'spin-holding' field (0.3-T or 1.1-T) aligned with the nominal beam direction, or a vertical (70-G or 110-G) spin-precessing field. The longitudinal field quenched muon depolarization in muonium via the Paschen-Back effect. The data collected with the longitudinal field were used to measure the rate at the spectrum endpoint. The data collected with the spin-precessing field, after the appropriate cuts on muon decay time, were equivalent to the unpolarized, i.e. P_μ=0, data. In this analysis these data were used for the momentum calibration of the spectrometer.

The angular acceptance for positrons was significantly increased by the downstream portion of the solenoid, which served as a 0.5 T-m solenoidal field lens. The solenoid lens focused the decay positrons

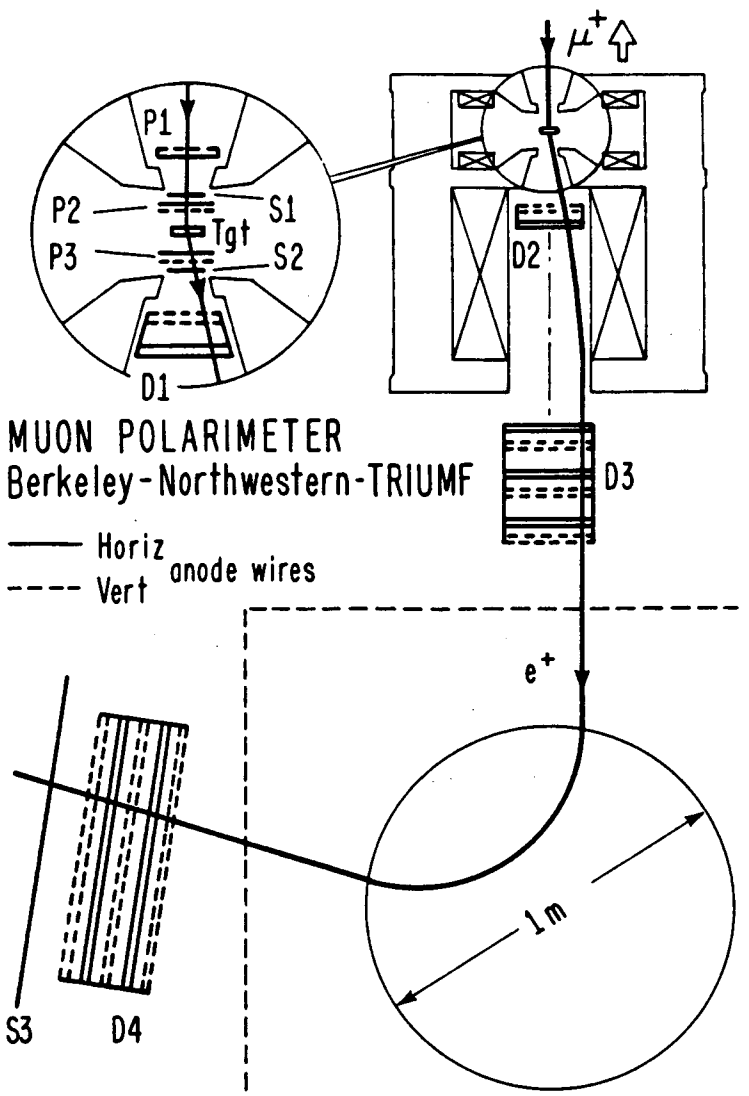

XBL 834-147

FIG. III.1. Plan view of muon polarimeter. P1-P3 are proportional chambers; S1-S3 are scintillators; D1-D4 are driftchambers. The veto scintillators V1 and V2 surrounding S1 and S2 respectively are not shown. Muons entering the solenoid are stopped in the target (Tgt). Decay e^+ emitted near the beam direction are focused by the solenoid onto the spectrometer.

onto the dipole magnet spectrometer. The septum between the target and solenoid bore made the focal length of the solenoid lens nearly independent from the choice of target field orientation.

The horizontally-focusing spectrometer was chosen in order to achieve a high momentum resolution and to maintain a large angular acceptance for positrons in combination with the solenoid. The volume between the spectrometer conjugate focal planes was evacuated. The vacuum windows were positioned close to the focal planes to minimize the adverse effects of Coulomb scattering on momentum resolution.

Particle trajectories in the target region (see inset of Fig. III.1) were measured by the proportional chambers P1 and P2 for muons, and by the proportional chamber P3 and driftchambers D1 and D2 for positrons. Positron trajectories outside the spectrometer focal planes were measured by the driftchambers D3 and D4. The scintillation counters S1, S2 and S3 provided trigger signals.

The data were accumulated in three running periods (to be denoted by Run 1, etc.) at the TRIUMF cyclotron during 1982-84. The experimental conditions were essentially the same for all three running periods, except for minor differences mentioned below and in Appendix A. The longitudinal field in the stopping target region was 1.1-T for Runs 1 and 2, and 0.3-T and 1.1-T for Run 3. A total of $1.8 \cdot 10^7$ ($1.4 \cdot 10^7$) triggers were collected in the spin-holding (spin-precessing) mode on 130 (170) computer tapes (1600 BPI). Under the optimal conditions these data would have been accumulated in ~20 continuos days of running time. In each of the three running periods

the data were also collected in many special runs to be described in section IV. The data collected in these special runs were used for the momentum calibration of the spectrometer.

The "surface" muon beam, muon polarimeter and the trigger will be described in greater detail below. We will also briefly review the process of muon deceleration to thermal energies and the suppression of muon depolarization in muonium by the longitudinal field.

III.B. The Beamline

The experiment utilized the M13 beamline[26] at the TRIUMF meson facility. M13 is a low energy (20-130 MeV/c) muon and pion channel, which views a 2 mm or a 10 mm thick carbon production target at 135° with respect to the primary proton beam (see Fig. III.2). The particles are transported in vacuum through two 60°-bending dipoles, with momentum-selecting slits at the two foci allowing a momentum bite $\Delta p/p$ as low as 0.5%. The beamline was tuned to deliver about 15,000 μ^+ per second in a 1% momentum interval at a typical proton beam current of 100μA. The particles were focused in a narrow 0.3 msr cone on a ~1 cm radius spot at the muon stopping target.

Positive particle fluxes in the beamline, obtained in beam tuning studies of Ref. 26, are shown in Fig. III.3. Just below 29.8 MeV/c the muon flux is dominated by "surface" muons, produced by pions decaying at rest near the surface of the production target. In the experiment the beamline was tuned to 29.5 MeV/c, just below the surface muon edge. At this beamline setting the surface muons

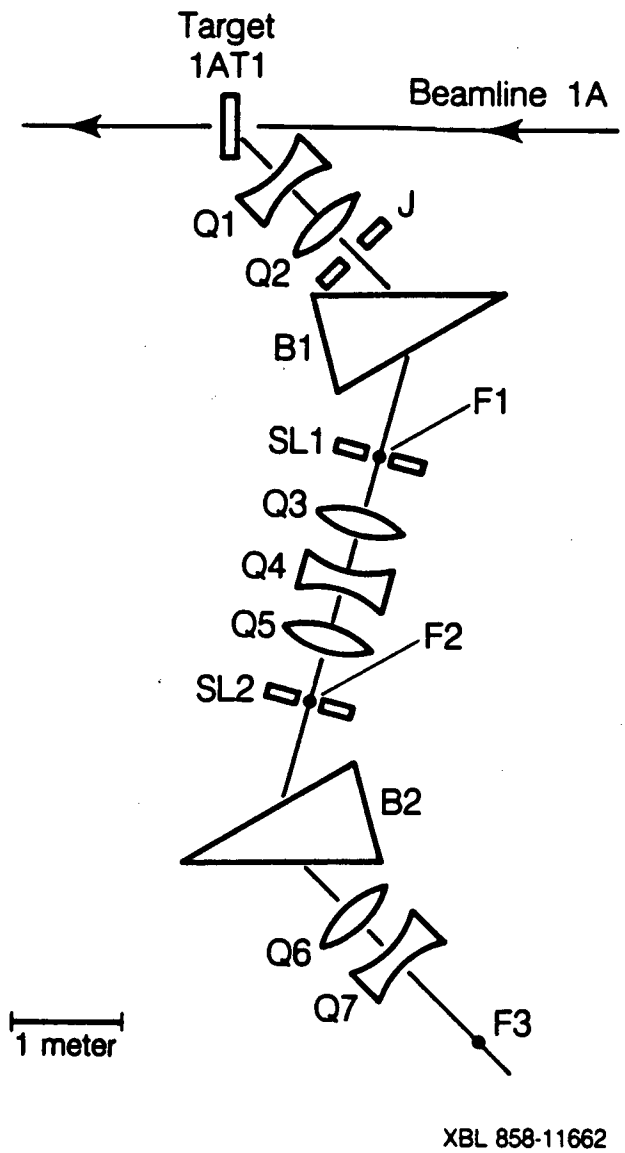

FIG. III.2. The M13 beamline at TRIUMF. B1 and B2 are dipoles; Q1-Q7 are quadrapoles; F1-F3 are foci; the slits SL1 and SL2, and the jaws J have both horizontal and vertical components.

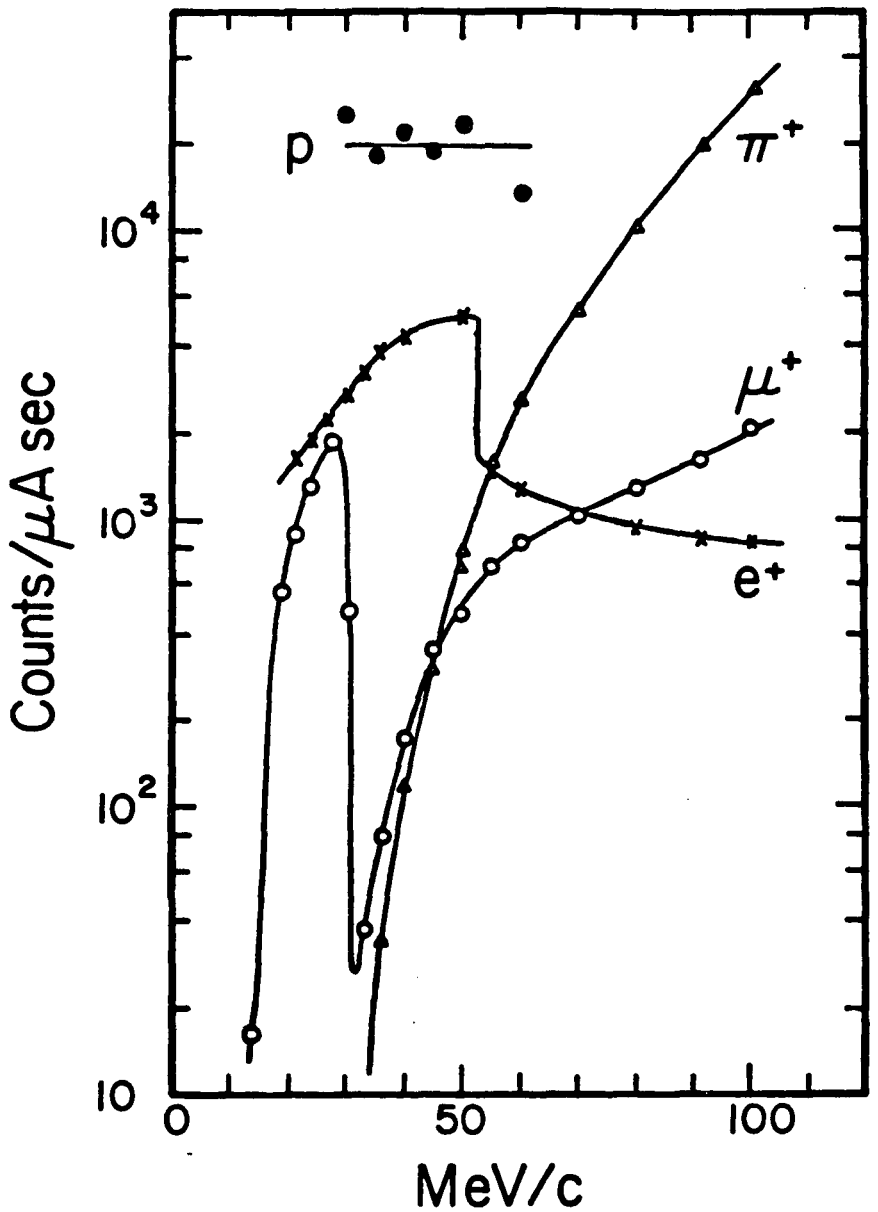

FIG. III.3. Positive particle fluxes versus beamline momentum settings in the M13 beamline at TRIUMF (taken from Ref. 26). The data was collected with all slits and jaws in the beamline fully open.

constitute over 98% of the muon flux. In the absence of right-handed currents and scattering they are expected to be fully polarized. The remaining 1.5% component of the muon flux at this beamline setting consists of "cloud" muons, produced by pions decaying in flight. The cloud muons are not highly polarized, and hence were removed from the event sample.

The cut to eliminate cloud muons was made possible by the pulsed structure of the primary proton beam. At TRIUMF protons bombard the primary target at 43 ns intervals. The cloud muons must be produced in close proximity to the production target, i.e. promptly within few ns of the 2-5 ns beam bursts, if they are to be transported by the M13 beamline. Since the production of cloud muons is restricted to a small time interval in the 43 ns cycle, they could be eliminated from the event sample by a cut on particle arrival time at the stopping target with respect to the cyclotron RF signal.

The rate of particle arrival at the stopping target with respect to the cyclotron RF signal is shown in Fig. III.4 for the beamline settings of 29.5 MeV/c and 30.5 MeV/c. For the beamline setting of 29.5 MeV/c (Fig. III.4a), the arrival rate is dominated by the surface muons, which results in an exponential time distribution corresponding to the pion lifetime. For the beamline tuning of 30.5 MeV/c (Fig. III.4b), there are two isolated peaks corresponding to the cloud muons and pions. The cloud muons and pions were eliminated from the event sample by a timing cut, shown by the shaded regions in Fig. III.4.

Aside from muons and pions, the other particles in the beamline

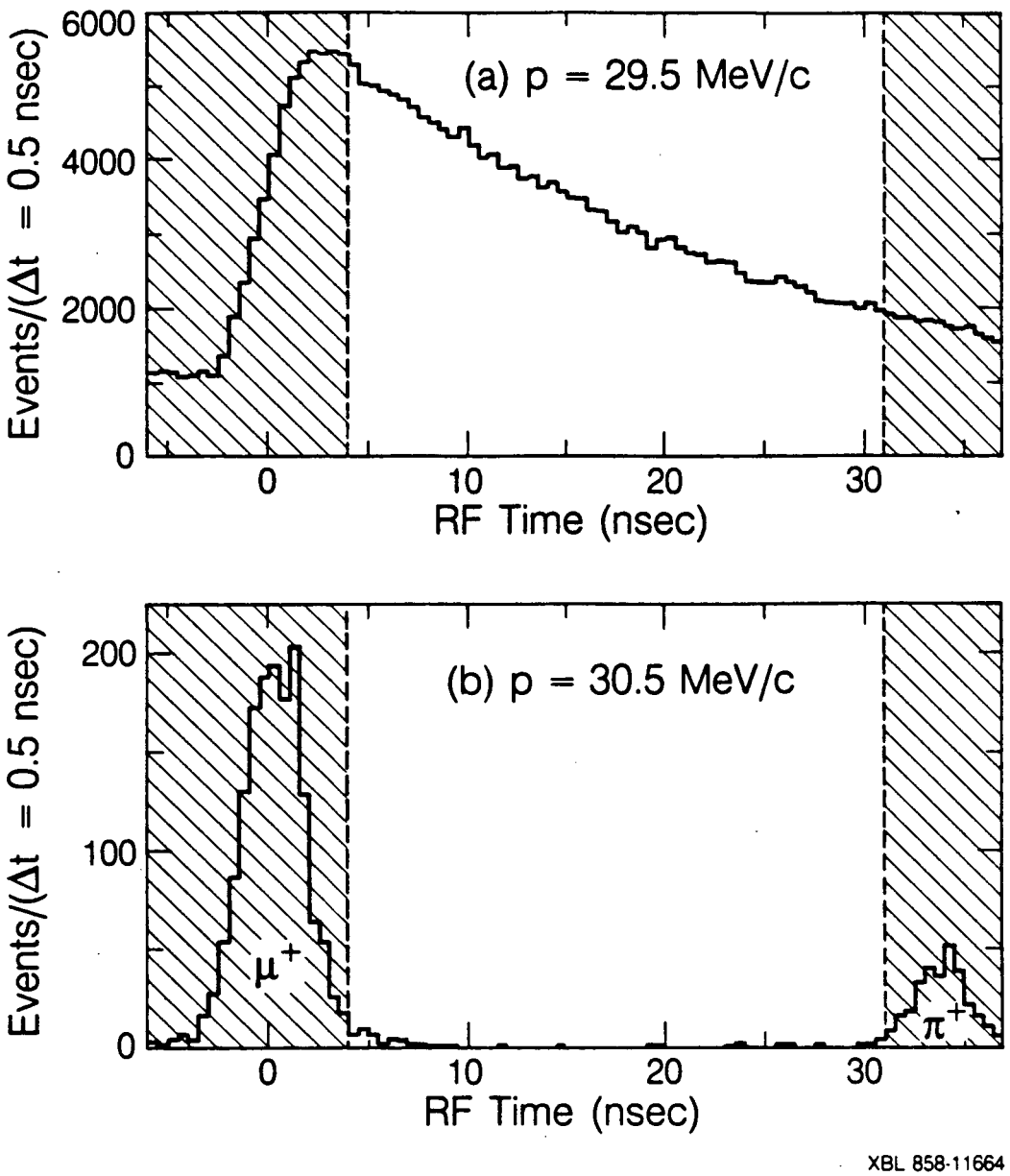

FIG. III.4. Beam particle arrival times at the stopping target with respect to the cyclotron RF cycle at (a) 29.5 MeV/c and (b) 30.5 MeV/c. The shaded regions, containing almost all of the cloud μ^+ and prompt π^+ contaminations, were rejected.

are protons and positrons. Protons stopped in the beamline vacuum window and did not reach the detectors. Positrons passed through the stopping targets and therefore were rejected by the trigger requirement.

III.C. Muon Deceleration and Thermalization

Before describing the muon slowing down process, let us briefly review the suppression of muon depolarization in muonium by the longitudinal magnetic field aligned with the nominal beam direction. The magnetic field direction will define the axis of quantization. The energy eigenstates of muonium will be expressed in terms of a variable $y=|B|/(1585\ \mathrm{G})$, and a "natural" basis $|m_\mu m_e\rangle$:

$$|{++}\rangle$$

$$s|{+-}\rangle + c|{-+}\rangle$$

$$c|{+-}\rangle - s|{-+}\rangle$$

$$|{--}\rangle$$

where the compact notation $|{+-}\rangle$ means $|m_\mu=+1/2, m_e=-1/2\rangle$, etc., and

$$c=(1/\sqrt{2})\ [1+\ y(1+y^2)^{-\frac{1}{2}}\ ]^{\frac{1}{2}} \qquad s=(1/\sqrt{2})\ [1-\ y(1+y^2)^{-\frac{1}{2}}\ ]^{\frac{1}{2}}\ .$$

For simplicity, suppose that all muons arrive with a spin parallel to the field. Then half of the muonium ensemble is formed in the state $|{++}\rangle$ and half in the state $|{+-}\rangle$. The state $|{++}\rangle$ is stationary, and hence the muon polarization of half of the ensemble is preserved. The polarization for the other half of the ensemble oscillates between

$$P_\mu=(c^2-s^2)^2-4s^2c^2=(y^2-1)(y^2+1)^{-1}$$

and $P_\mu=1$ with a frequency $\omega=2.3(1+y^2)^{\frac{1}{2}}$ GHz. The net polarization is thus $P_\mu=(1/2)(2y^2+1)(y^2+1)^{-1}$, and therefore the magnetic field reduces muon depolarization in muonium to $(1/2)(1+y^2)^{-1}$.

Muons reached the stopping target with a kinetic energy of ~3.3 MeV, after traversing 50 mg/cm^2 of material (mostly windows, wires and gas) upstream of the target. The main energy-loss processes, as μ^+ slows down to thermal velocities, depend on the μ^+ kinetic energy.[27] For kinetic energies E>2-3 keV the energy loss is due to scattering with electrons, and μ^+ are partially depolarized through spin exchange with the unpolarized electrons of the medium.[28] A correction to the result for $\xi P_\mu \delta/\rho$ due to such depolarization will be computed in section VI.C. At E≈2-3 keV the μ^+ velocity is comparable to that of the valence electrons of the medium, and muons begin to capture and lose electrons rapidly, forming a succession of short-lived muonium (μ^+e^-) states. Again, energy is lost in collisions with electrons. Below E≈200 eV the energy loss is due to collisions of a stable muonium atom with atoms and molecules. The time spent by the decelerating μ^+ in muonium states (~10^{-12} sec) is too short for the hyperfine transitions to cause any appreciable depolarization.

The state in which μ^+ is finally thermalized depends on the medium. In many non-metals muons are thermalized as muonium. In metals, however, the μ^+ are thermalized in a quasi-free state, because the high conduction electron concentration effectively screens the μ^+ from interactions with individual electrons. For this

reason most of our data was collected with high-purity (≥99.99%) metal foils (Ag,Al,Au,Cu) as stopping targets (target thicknesses are tabulated in Appendix A). A small amount of data was collected with liquid He, where muonium is disfavored in the final state due to a large difference between the ionization potential of He (24.6 eV) and muonium (13.5 eV). The energetically favored final state in liquid He (in which the μ^+ polarization is preserved) is the molecular ion $He\mu^+$ with binding energies[29] of 1.9 eV for the ground state and 1.2 eV for the first vibrational state. (We were therefore surprised to find in our experiment that liquid He is 12% depolarizing without the strong longitudinal field.[12] A possible explanation is that if muons are thermalized as muonium, they survive in this form for a considerable time because of the improbability of encountering a He^+ ion with which to recombine as $He^+ + \mu^+e^- \rightarrow He\mu^+$.)

Although the strong longitudinal field is sufficient to quench μ^+ depolarization in muonium, it cannot 'hold' the spins of quasi-free muons in metal targets. The energy difference between states where the muon spin is parallel or anti-parallel to the 1.1-T (0.30-T) field is only $\Delta E = 6.2\times10^{-7}$ eV (1.7×10^{-7} eV), while the room temperature thermal energy is $kT = 2.6\times10^{-2}$ eV. Relaxation of the muon spins toward the equilibrium situation, where the number of spins parallel or anti-parallel to the applied field are almost equal, requires the presence of oscillating magnetic fields with frequency $\omega = 9.4\times10^8\ s^{-1}$ for 1.1-T longitudinal field ($2.6\times10^8\ s^{-1}$ for 0.30-T). Such fields may be provided by the nuclear magnetic dipole moments. The stopped muon polarization would then decay

exponentially towards thermal equilibrium with the characteristic spin-lattice relaxation time T_1. In section V we will look for possible evidence of spin relaxation by comparing the results for $\xi P_\mu \delta/\rho$ from different time intervals.

III.D. The Muon Polarimeter

The muon polarimeter is shown schematically in Fig. III.1. Muons traversed about 50 mg/cm^2 of material before being stopped in metal foil or liquid He targets, placed on the axis between the first two coils of the solenoid magnet. The solenoid magnet served two purposes. The front portion produced a 0.30-T or 1.1-T longitudinal spin-holding field aligned with the nominal beam direction. The strong longitudinal field quenched muon depolarization in muonium. The back portion, with a bore of 11-cm radius, served as a 0.5 T-m solenoidal field lens, focusing the decay positrons onto the dipole magnet spectrometer. The iron configuration in the stopping target region was designed to produce nearly axial field. The cosine of an angle between the field and the solenoid axis was >0.99999 in the fiducial target area.

The experiment was run in two modes, corresponding to two different field orientations in the target region. In the spin-holding mode a strong longitudinal field was applied to suppress muon depolarization. The spin-held data were used to measure the decay rate at the endpoint. In the spin-precessing mode, the longitudinal field was nulled to within ±2 G, and a 70-G or 110-G

vertical field, transverse to the beam direction, was applied. The vertical field was produced by an additional water-cooled Cu coil, consisting of four horizontal sections transverse to the beam direction. In the transverse field of 70 (110) G the muon spins precessed about the vertical axis at a frequency of 0.95 (1.5) MHz. After appropriate cuts on muon decay time, the spin-precessed data is equivalent to the unpolarized, i.e. $P_\mu=0$, data, and hence it is used here for the momentum calibration of the spectrometer.

The residual longitudinal field in the target region was nulled to within ±2 G by means of a small reverse current applied to the upstream solenoid coils. The null condition was indicated by the maximal ratio of events to stopped μ^+ in Run 1, and by field measurements in Runs 2 and 3.

The primary design goal of the positron spectrometer was to achieve a high momentum resolution, while maintaining an acceptance of ≥250 msr in combination with the target solenoid. In order to minimize the adverse effects of multiple Coulomb scattering on momentum resolution, a horizontally focusing spectrometer was chosen, which bent the x=1 e^+ trajectories by 98°. The 37 in. diameter dipole magnet with approximate cylindrical symmetry (originally used by Sagane et al.[30]) provided nearly symmetric point-to-point focusing for particles originating in a focal plane at a distance of ~1 m from the center of the magnet. The volume between the conjugate focal planes was evacuated and the vacuum windows were positioned close to the focal planes.

The combined solenoid lens-spectrometer magnet system accepted

particles over a ±15% momentum range and decay angles relative to the solenoid axis of $\cos\theta>0.95$. In the final analysis we use events only from a sub-portion of this phase space.

The spectrometer magnet was powered continuously, and the NMR-monitored central field of 0.32-T drifted by less than one gauss over a period of several weeks. The absolute momentum calibration of the spectrometer was obtained from the position of the x=1 edge in the spin-precessed data, and subsequently this calibration was used to fit the spin-held data. To minimize the effect of a drifting spectrometer field and other possible drifts on the x scale calibration, the target field was switched approximately hourly between the spin-holding and spin-precessing orientations. The residual longitudinal field was nulled each time the change was made to the spin-precessing mode.

Particle trajectories in the target region (see inset of Fig. III.1) were measured by the proportional chambers P1 and P2 for the incoming muons, and by the proportional chamber P3 and driftchambers D1 and D2 for the outgoing positrons. The scintillation counters S1 (0.005 in. thick), just upstream of P1, and S2 (0.010 in. thick), just downstream of P3, provided the trigger signals. The thickness of the scintillation counter S1 was kept to a mimimum to minimize the chance of a muon stopping upstream of the target. The veto scintillation counters V1 and V2 (0.125 in. thick), just in front of S1 and behind S2 respectively, had 1.5 in. diameter aperture-defining holes around the solenoid axis. All scintillation counters were viewed from left and right by photomultipliers.

Positron track coordinates outside the spectrometer focal planes were measured by low mass driftchambers D3 and D4. A scintillation counter S3 was placed behind the chamber D4 to provide trigger signals.

The proportional chambers and driftchambers were run on methane-8% methylal gas mixture, selected to minimize Coulomb scattering. Chamber resolutions and efficiencies will be discussed in section IV on event reconstruction.

III.E. The Trigger

The trigger logic was based on fast signals from the scintillation counters and the cathode planes of the proportional chambers. A trigger required the signature of a particle stopping in the target, followed, in delayed coincidence of 0.1-10 μs, by a positron, registered by detectors downstream. With detector signals denoted by their symbols in Fig. III.1, the trigger requirement was $P1 \cdot \overline{V1} \cdot S1 \cdot P2 \cdot \overline{P3} \cdot \overline{S2} \cdot \overline{V2}$ in delayed coincidence with $P3 \cdot S2 \cdot S3 \cdot \overline{V1} \cdot \overline{V2}$. The scintillation counter S1 had a greater amount of material in the muon path than did the proportional chamber P2, and consequently it was placed upstream of P2 to minimize the probability of a muon stopping in the last detector element required for the muon part of the trigger. The high voltage on the scintillation counter S1 was set to make it efficient for muons, but not for the beam positrons, which deposited 8 times less energy.

Events were tagged if a particle was detected upstream of the

stopping target within 0.3-10 μs after a muon stop. Such events had a high probability for the decay positron being produced by an extra muon in the target, rather than the muon causing the trigger. These events were rejected in analysis if the extra particle was detected before the decay positron.

Beam positrons, which constitute ~60% of the M13 beam flux for the beamline setting of 29.5 MeV/c, passed through the stopping targets and apparatus, and were stopped in lead shielding next to the low momentum side of the vacuum tank in the spectrometer magnet. The beam positrons did not satisfy the particle stop requirement, and only an insignificant fraction of them reached the S3 counter to mimic decay positrons. The beam momentum of 29.5 MeV/c was much lower than the minimum positron momentum of 49 MeV/c for events used in the data analysis. Hence, beam positrons did not constitute a background.

IV. EVENT RECONSTRUCTION AND SELECTION

Track reconstruction was relatively simple since there was only one incoming and one outgoing track, and all wire chamber planes were over 90% efficient with little noise. However, special attention had to be paid to the reconstruction of curved tracks in the solenoid magnet. The curved tracks were fitted using the first-order optics approximation for the cylindrically symmetric fields, as described below.

Initially all e^+ track segments were fitted with straight lines. Positron track segments were found separately in the horizontal and vertical projections in the 3 groups of wire chamber planes (refer to Fig. III.1): P3, D1, D2 (5 vertical and 5 horizontal wire planes), D3 (6 and 6), and D4 (6 and 4). All possible hit combinations were considered, and a track with a minimum chi-square was selected among those that had hits in the maximum number of planes. A combination of hits was considered to be a track if the total χ^2 was below a maximum value corresponding to a hit accuracy of ~1 mm in D3 and D4 and ~2 mm in P3 through D2.

In 99% of the triggers tracks were found in all six segments. 13% of the triggers were rejected to avoid ambiguities due to high or low hit multiplicities associated with the μ^+ or e^+ track. To achieve greater accuracy in the $\cos\theta$ measurement positron tracks were required to have unambiguous hits in both the horizontal and vertical planes of P3, and at least 3 hits were required in each projection of the e^+ track inside the solenoid. 95% of events in the final sample

had the e^+ track portion inside the solenoid recorded by at least 9 wire planes.

Muon tracks were accepted if they were unambiguous, or if there were no more than two hits in one and only one of the P2 planes. In the latter case (5% of the final sample) we selected the track which in extrapolation to the stopping target was closest to the decay vertex indicated by the e^+ track extrapolation.

Track segments in the solenoid were then refitted in both projections simultaneously in the first-order optics approximation for cylindrically symmetric fields.[31] In this approximation particle trajectories through the solenoid are determined from initial conditions by means of transfer matrices, computed from magnetic rigidity and field values on the solenoid axis. Curved tracks could therefore be fitted without detailed step-by-step computation of orbits in the magnetic field. Incoming and outgoing tracks were extrapolated to the stopping target, so that the track angles could be determined at the decay vertex. It was found in the Monte-Carlo simulation based on propagating the particles through the magnetic field in small steps that, in the absence of scattering and chamber resolution effects, $\cos\theta$ was determined extremely accurately using the first-order optics approximation (see section VII.D).

The non-linear time-distance relationships in the driftchambers were obtained separately for each plane of every chamber. All chamber planes were aligned in the transverse direction; the residual means were less than 50μ. In the initial approximation the time-distance relationships were found by integrating the flux and

assuming uniform cell illumination. They were then dynamically fine-tuned by making small adjustments based on track residuals. The procedure converged after 1500 events. Curved tracks were fitted in the first-order optics approximation. Residuals of $\sigma<500\mu$ were achieved in D1 and D2, with the exception of two planes in D1 where σ was $\approx 700\mu$. Residuals in D3 and D4 had $\sigma<250\mu$.

All proportional chambers had 2mm wire spacings, with up to 3 consecutive wires considered as a single acceptable hit. Events with 4 or more consecutive wires hit were rejected.

Positron tracks were required to link in the following extrapolations: inside the solenoid magnet, both in radial and azimuthal positions; in vertical slope and vertical position inside the spectrometer magnet; and in impact parameter with respect to the central axis of the approximately cylindrically symmetric field of the spectrometer. Muon and positron extrapolations to the decay vertex at the stopping target were required to match within 4 mm radius. Track linkage requirements resulted in a 30% loss of events. Events near the edges of geometrical acceptance were cut to avoid particles that were scattered back into the apparatus (20% event loss). Other small fiducial cuts were made to insure event unambiguity.

The horizontal focusing property of the spectrometer allowed the e^+ momentum to be reconstructed from the sum of horizontal coordinates at the two conjugate focal planes. This sum was empirically corrected with momentum-dependent first or second-order terms in three variables: mean vertical deviation from the median

plane of the spectrometer, impact parameter with respect to spectrometer axis, and vertical position at the spectrometer exit. Initially, the corrections were obtained from special calibration runs, when beamline momentum bite was reduced to 0.5% $\Delta p/p$, and straight-through beams of positrons, in 3 to 5% steps in momentum, passed through the apparatus. The corrections were then fine-tuned by requiring the edge position in unpolarized, i.e. spin-precessed, data to be identical for every portion of spectrometer phase-space, partitioned in the above mentioned three variables. For calibration purposes, the spin-precessed data were collected at several values of spectrometer current, varying by -15 to +5% from the optimum in 3 to 5% steps. Momentum resolution achieved was approximately Gaussian, with $\sigma \approx 0.13\%$.

Momentum dispersion of 1.056±0.008% was obtained from the straight-through calibration runs taken with spectrometer currents varying from 42 to 100% of the optimal current in five 15 to 20% steps, and also from the edge positions found in runs at different settings of spectrometer current. The uncertainty in dispersion is based on agreement between five calibration curves, obtained at different times during the three data-taking runs.

V. DATA ANALYSIS

The analysis exploited the fact that near the endpoint the muon decay spectrum can be expressed as a linear combination of two pure V-A spectra, one with $P_\mu \cos\theta=0$, and another with $P_\mu=\cos\theta=1$. This is discussed in section II. The relevant equations are (2.2), (2.5) and (2.6). The result for $\xi P_\mu \delta/\rho$ was extracted from the rate at the spectrum endpoint $r(\theta)$, given by equation (2.5).

Fitting was performed with a double-precision version of the MINUIT program, and was based on minimizing the maximum-likelihood Poisson statistics χ^2, defined by

$$\chi^2=2\sum[e_i-o_i+o_i \ln(o_i/e_i)]$$

where o_i and e_i are the observed and expected number of events respectively for the ith bin.

The data were fitted separately in five $\cos\theta_e$ bins as explained below. For each $\cos\theta_e$ bin the fitting proceeded in two stages. First, the spin-precessed data were fitted to calibrate the spectrometer and determine its resolution and acceptance functions. The position of the x=1 edge in the spin-precessed data determined the location of the x=1 point on the reconstructed momentum scale; the edge sharpness determined the spectrometer momentum resolution. In the second stage, the spin-held data were fitted using the parameters found in the fit of the spin-precessed data. We now consider the fitting procedure in detail.

V.A. The Fitting Procedure

Here we describe the fitting performed for each of the five $\cos\theta_e$ bins.

For the spin-precessed data, cuts on muon decay time were adjusted to obtain an equivalent of the unpolarized, i.e. $P_\mu=0$, data sample. The resulting unpolarized spectrum, binned in x bins 0.001 wide (see Fig. V.1), was fitted from x=0.93 to x=1.01 as

$$N_1 S_{V-A}(x,0)A(x) \tag{5.1}$$

where N_1 is a free normalization, and $S_{V-A}(x,0)$ is the pure V-A decay spectrum with $P_\mu\cos\theta=0$. A(x) is a quadratic acceptance function given by

$$A(x)=1+B_1(1-x)+B_2(1-x)^2 \ , \tag{5.2}$$

where the linear and quadratic coefficients B_1 and B_2 are also free parameters.

If $\tilde{\rho}$ [i.e. $1-(4/3)\rho$] is non-zero, the unpolarized spectrum does not match the V-A unpolarized spectrum $S_{V-A}(x,0)$, and the acceptance function (5.2) will absorb the difference in spectral shapes. As a result, the linear coefficient B_1 in equation (5.2) gets a systematic shift of $+6\tilde{\rho}$, and a quadratic coefficient B_2 a shift of $(6B_1-12)\tilde{\rho}$. The world-average value of $\tilde{\rho}$ is $-.0023\pm.0035$. Fortunately, an error in B_1 (B_2) propagates into an error in $\xi P_\mu\delta/\rho$ with a factor of 10^{-3} ($1.5\cdot10^{-5}$), and hence this effect can be ignored.

The fitting function (5.1) was smeared to reflect spectrometer resolution and positron energy-loss straggling in the target (the amount of target material in positron path varied from 23 to

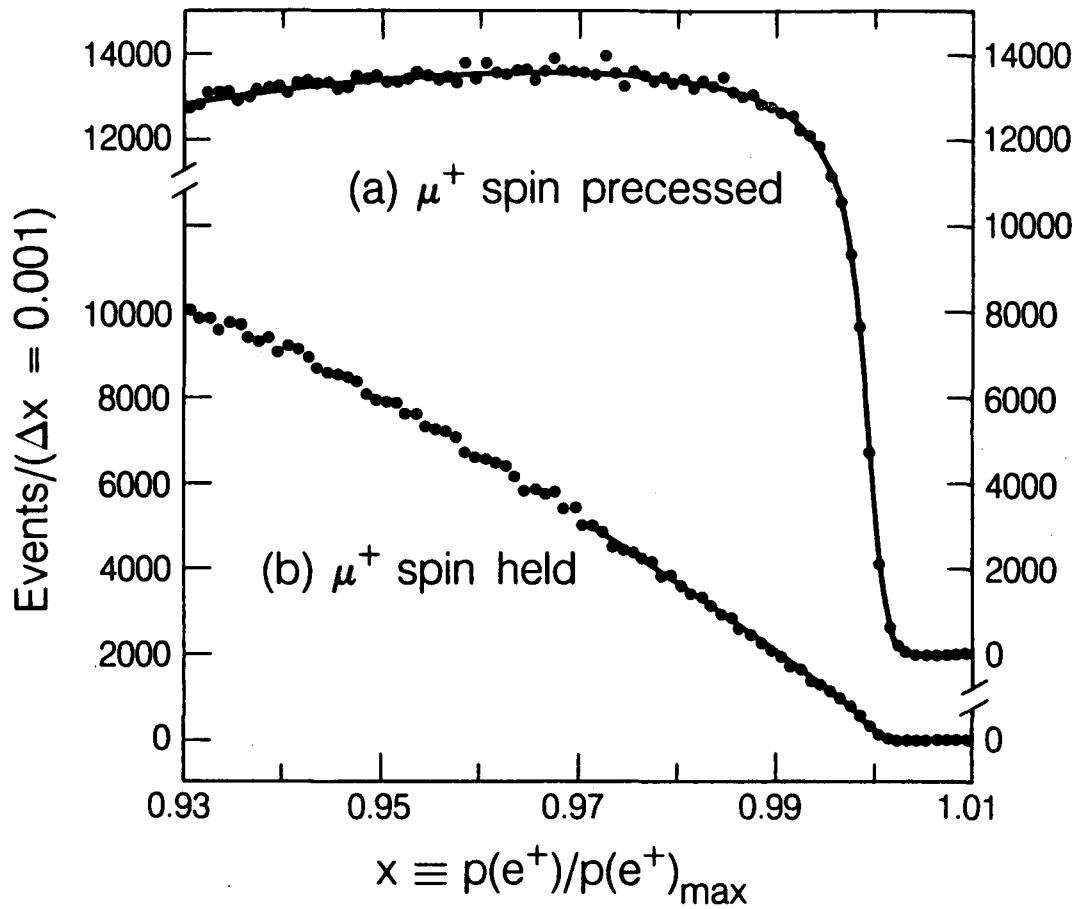

XBL 8512-11759

FIG. V.1. Measured positron spectra for (a) spin-precessing mode and (b) spin-holding mode. x is the reduced positron momentum. The solid curves show the fitted x ranges (x>.93 for the spin-precessed and x>.97 for the spin-held data). The edge in (a) corresponds to a resolution with gaussian part of <.15% rms. The spectra shown contain the data from all targets. Fits were performed for each target separately in 5 $\cos\theta_e$ bins, as described in the text.

170 mg/cm^2; see Appendix A) and in ≈200 mg/cm^2 of material downstream up to the spectrometer vacuum tank window.

The spectrometer (i.e. x) resolution was parametrized by a normalized sum of three gaussians with standard deviations σ, $\sqrt{3}\sigma$ and 3σ. The $\sqrt{3}\sigma$ and 3σ gaussians were introduced in order to obtain a better fit to the tails of the resolution in x, and they usually had small coefficients in the normalized sum. The resolution σ was typically 0.13%. The result for $\xi P_\mu \delta/\rho$ was relatively insensitive to the number of free parameters in the resolution function, changing by less than 10^{-4} when a single gaussian was used rather than all three.

There were a total of 7 free parameters in the fit of the spin-precessed data: the normalization N_1, the linear and quadratic coefficients B_1 and B_2 in the acceptance function, the 3 resolution parameters, and the position of the x=1 point on the reconstructed momentum scale.

Despite the large momentum acceptance of the apparatus, the spin-precessed data were fitted only from x=0.93 and the spin-held data only from x=0.97. A short extension of the x range below x=0.93 for the spin-held data had no effect on the result for $\xi P_\mu \delta/\rho$. A significant extension would have required more free parameters to fit acceptance, and would not have led to a decrease in the statistical error on $\xi P_\mu \delta/\rho$. The situation was similar for the spin-held data. Here the extension of the x range below 0.97 would have required an introduction of a free parameter to represent a possible difference in acceptance between the spin-precessed and spin-held data sets. Since the acceptance parameters correlated with $r(\theta)$, the rate at the

endpoint, the statistical error on $\xi P_\mu \delta/\rho$ would have increased. Furthermore, the systematic error due to possible differences in x acceptance between the two data sets increased quadratically with the x range for the fit of spin-held data. The range $x \geq 0.97$ for the spin-held data was optimal for the smallest combined (i.e. statistical and systematic) error.

The spin-held data, also shown in Fig. V.1, were fitted using the values for the x acceptance, x resolution and x=1 calibration point found for the spin-precessed data. In the second stage of fitting the two data sets were fitted simultaneously to allow the uncertainties in the x=1 calibration and x acceptance to contribute (~3% of the error) to the statistical error on $\xi P_\mu \delta/\rho$. Since the resolution in x was determined primarily by the sharpness of the x=1 edge in the spin-precessed data, the resolution parameters in the combined fit were fixed to the values found when the spin-precessed data were fitted alone. Fixing the resolution parameters shortened the overall computer time required by a factor of 3. It was checked that fixing the resolution parameters in the combined fit did not affect either the result or the errors on $\xi P_\mu \delta/\rho$.

In the combined fit the spin-precessed data were fitted to the same function (5.1) as before, except that the resolution parameters were fixed. The spin-held data, also binned in x bins 0.001 wide (see Fig. V.1), was fitted according to equation (2.2), from x=0.97 to x=1.01, as

$$N_2[(1-r(\theta))S_{V-A}(x,1)+r(\theta)S_{V-A}(x,0)]A(x) \qquad (5.3)$$

where N_2 is a free normalization, $S_{V-A}(x,1)$ and $S_{V-A}(x,0)$ are the

pure V-A spectra at $P_\mu\cos\theta=1$ and $P_\mu\cos\theta=0$ respectively, A(x) is the quadratic acceptance function (5.2), and the free parameter $r(\theta)$ is the relative rate at the endpoint. The function (5.3) was smeared in the same manner as for the spin-precessed data to reflect the spectrometer resolution and positron energy-loss straggling.

There were a total of 6 free parameters in the combined fit. They were the x=1 calibration point, N_1, B_1, B_2, all determined primarily by the spin-precessed data, and N_2, $r(\theta)$, determined by the spin-held data.

The result for $\xi P_\mu\delta/\rho$ was extracted from $r(\theta)$, which, according to the equation (2.5), is just $1-(\xi P_\mu\delta/\rho)\cos\theta$. Since the data were fitted in subsets in which the variation in $\cos\theta$ was much greater than the error on $r(\theta)$, and since any error in $\cos\theta$ propagates into the same error in $\xi P_\mu\delta/\rho$, we must consider the question of what value should be assigned to $\cos\theta$ under such circumstances. We rewrite $r(\theta)$ as

$$r(\theta_{av})=1 - \xi P_\mu\frac{\delta}{\rho}\cos\theta_{av}. \tag{5.4}$$

The complication is that $\cos\theta_{av}$ is not just $\cos\theta$ averaged over the data, as will be explained in section V.B.

Let us mention here the main point of that section: $\cos\theta_{av}$ was computed from $\cos\theta_\mu\cos\theta_e$ averaged over the spin-held data. Here θ_μ and θ_e are the polar angles with respect to the solenoid axis for muons and positrons respectively. Since muon spins precessed about the solenoid axis very rapidly (40 Mhz for 0.3-T longitudinal field and 150 Mhz for 1.1-T) compared to the muon lifetime τ_μ=2.2 ns, one

may think of $\cos\theta_\mu\cos\theta_e$ as $\cos\theta$ averaged over one spin-precession period ($T \ll \tau_\mu$):

$$\cos\theta_\mu\cos\theta_e = -(1/T)\int_0^T \hat{s}_\mu(t)\cdot\hat{p}_e dt \tag{5.5}$$

where $\hat{s}_\mu$ and $\hat{p}_e$ are the unit vectors corresponding to the muon spin and positron momentum respectively. Two small corrections had to be added to the data-averaged $\cos\theta_\mu\cos\theta_e$. They will be discussed in section VI. The reader who does not wish to follow a rather involved discussion in section V.B may now proceed directly to section V.C summarizing the analysis method.

V.B. Computation of $\cos\theta_{av}$

Recall that in the expression for the muon decay spectrum $\cos\theta$ was defined as $-\hat{s}_\mu\cdot\hat{p}_e$, where $\hat{s}_\mu$ and $\hat{p}_e$ are the unit vectors corresponding to the directions of muon spin and positron momentum at the μ^+ decay vertex. At the π^+ decay vertex the muon spin is parallel or anti-parallel to the muon momentum (massless neutrinos have been assumed; μ^+ helicity is always -1 for V-A). For the the moment let us ignore the effects of scattering, finite chamber resolution and finite accuracy of track extrapolation. The corrections to $\cos\theta_{av}$ due to these factors will be considered in section VI. Therefore, we can assume that the spin direction of muon when it enters a stopping target is given by the extrapolation of the measured muon track, and similarly that the direction of the positron momentum at the decay vertex is given by the extrapolation of the

measured positron track.

Let θ_μ, ψ_μ and θ_e, ψ_e be the polar and azimuthal angles with respect to the longitudinal field axis for $-\hat{s}_\mu$ (the minus sign is put in for convenience) and $\hat{p}_e$ respectively. Since muon spins precessed very rapidly in the strong longitudinal field, ψ_μ would have been difficult to measure. However, it was not necessary to measure ψ_μ, for it will be shown that it is sufficient to know just θ_μ.

To distinguish the spin direction $\hat{s}_\mu$ at the μ^+ decay vertex from the spin direction when a muon enters the stopping target, let us denote the former by $\hat{s}_{\mu,v}$ and the latter by $\hat{s}_{\mu,ent}$. We will ignore muon scattering in the stopping target, so that $\theta_{\mu,v}$ is identical to $\theta_{\mu,ent}$, and both will be denoted by θ_μ.

Our goal is to compute the positron spectrum for the spin-held data in terms of the theoretical decay rate, the angular and x acceptance functions, and the angular distribution of incoming muons. We will now show that for muons reaching a stopping target, the angular distribution of muon spins at the decay vertex, i.e. the $\hat{s}_{\mu,v}$ distribution, is independent of the azimuthal angle $\psi_{\mu,v}$.

Let $Q(\theta_\mu, \psi_{\mu,ent})$ describe the angular distribution of $\hat{s}_{\mu,ent}$ for muons reaching a stopping target, after all software cuts relevant to muons have been applied. Muon spins precess about the longitudinal field axis very rapidly (40 Mhz for 0.3-T and 150 Mhz for 1.1-T) compared to the muon lifetime τ_μ=2.2 μs. This implies that for a muon, arriving with the spin direction given by $(\theta_\mu, \psi_{\mu,ent})$, the probability of muon spin direction at the decay vertex being $(\theta_\mu, \psi_{\mu,v})$ is independent of $\psi_{\mu,v}$. Since the $\hat{s}_{\mu,v}$ angular

distribution, for the muons reaching a stopping target, is independent of $\psi_{\mu,v}$, it can be written as

$$R(\theta_\mu)= (1/2\pi)\int_0^{2\pi} Q(\theta_\mu,\psi_{\mu,ent})d\psi_{\mu,ent} \ .$$

It is important to distinguish the $\hat{s}_{\mu,v}$ distribution for the muons reaching a stopping target from the $\hat{s}_{\mu,v}$ distribution for events in the spin-held data. Although the former distribution is independent of $\psi_{\mu,v}$, the latter distribution does in fact depend on $\psi_{\mu,v}$ if the angular acceptance for positrons is ψ_e dependent. It is the former distribution, represented by $R(\theta_\mu)$, which will be needed for the computations below.

The muon decay spectrum may be written as

$$S(x,\cos\theta)=a(x)+b(x)\cos\theta \ .$$

For the spin-held data in one of the $\cos\theta_e$ bins, let $A(\theta_e,\psi_e,x)$ denote the total acceptance function for positrons, including the selection process bias (i.e. $\cos\theta_e$ must be in a certain range), the acceptance of the apparatus and software cuts. Ignoring statistical fluctuations, the positron spectrum $W(x)$ for the fitted subset of the spin-held data is given by

$$W(x) \sim \int[a(x)+b(x)\cos\theta]A(\theta_e,\psi_e,x)R(\theta_\mu)d\omega_e d\omega_\mu \qquad (5.6)$$

where $d\omega$ denotes the integration over the angular phase space, i.e. $d\omega_e=d(\cos\theta_e)d\psi_e$, and

$$\cos\theta=\cos\theta_\mu\cos\theta_e+\sin\theta_\mu\sin\theta_e\cos\psi_\mu\cos\psi_e+\sin\theta_\mu\sin\theta_e\sin\psi_\mu\sin\psi_e \ .$$

From now on ψ_μ always denotes $\psi_{\mu,v}$.

Let us make an assumption that x acceptance is independent of $\cos\theta_e$. In practice this was not true, and we will return to this

issue shortly. Under this assumption, $A(\theta_e,\psi_e,x)$ can be written as a product of two acceptance functions

$$A(\theta_e,\psi_e,x)=A(\theta_e,\psi_e)A(x) \ .$$

If the spectrum $W(x)$ is now fitted according to (5.3), $\cos\theta_{av}$ is defined by

$$N[a(x)+b(x)\cos\theta_{av}]A(x)= \int[a(x)+b(x)\cos\theta]A(\theta_e,\psi_e)A(x)R(\theta_\mu)d\omega_e d\omega_\mu \tag{5.7}$$

where N is the normalization. Hence

$$\cos\theta_{av}=\frac{\int A(\theta_e,\psi_e)R(\theta_\mu)\cos\theta d\omega_e d\omega_\mu}{\int A(\theta_e,\psi_e)R(\theta_\mu)d\omega_e d\omega_\mu} \ . \tag{5.8}$$

Note that $\cos\theta_{av}$ is <u>not</u> $\cos\theta$ averaged over the data, which is given by

$$\langle\cos\theta\rangle=\frac{\int\cos\theta[a(x)+b(x)\cos\theta]A(\theta_e,\psi_e)A(x)R(\theta_\mu)d\omega_e d\omega_\mu dx}{\int[a(x)+b(x)\cos\theta]A(\theta_e,\psi_e)A(x)R(\theta_\mu)d\omega_e d\omega_\mu dx} \ . \tag{5.9}$$

Since $R(\theta_\mu)$ is independent of ψ_μ, the ψ_μ-dependent terms in $\cos\theta$ vanish in (5.8) after integration over ψ_μ, and hence in (5.8) $\cos\theta$ can be replaced by $\cos\theta_\mu\cos\theta_e$

$$\cos\theta_{av}=\frac{\int\cos\theta_\mu\cos\theta_e A(\theta_e,\psi_e)R(\theta_\mu)d\omega_e d\omega_\mu}{\int A(\theta_e,\psi_e)R(\theta_\mu)d\omega_e d\omega_\mu} \ . \tag{5.10}$$

As mentioned above, one may think of $\cos\theta_\mu\cos\theta_e$ as $\cos\theta$ averaged over one spin precession period ($T\ll\tau_\mu$):

$$\cos\theta_\mu\cos\theta_e=-(1/T)\int_0^T\hat{s}_\mu(t)\cdot\hat{p}_e dt \ . \tag{5.5}$$

Since $A(\theta_e,\psi_e)$ was not known a priori, in the analysis $\cos\theta_{av}$ was computed from $\cos\theta_\mu\cos\theta_e$ averaged over the spin-held data

$$\langle\cos\theta_\mu\cos\theta_e\rangle = \frac{\int\cos\theta_\mu\cos\theta_e[a(x)+b(x)\cos\theta]A(\theta_e,\psi_e)A(x)R(\theta_\mu)d\omega_e d\omega_\mu dx}{\int[a(x)+b(x)\cos\theta]A(\theta_e,\psi_e)A(x)R(\theta_\mu)d\omega_e d\omega_\mu dx} . \tag{5.11}$$

Two corrections had to be added to $\langle\cos\theta_\mu\cos\theta_e\rangle$. One correction is due to the difference between $\langle\cos\theta_\mu\cos\theta_e\rangle$ computed from the measured tracks, and $\langle\cos\theta_\mu\cos\theta_e\rangle$ if it were computed from the true values of θ_μ and θ_e. This difference is due to scattering and finite chamber resolution. Since positron scattering depended on the target, this correction was target-dependent. The second correction compensated for the difference between $\langle\cos\theta_e\cos\theta_\mu\rangle$, given by (5.11), and the acceptance-weighted average $\cos\theta_e\cos\theta_\mu$, defined by (5.10). The second correction was target-independent. The computation of these corrections is described in section VI.

Let us now return to the issue of $\cos\theta_e$-dependent x acceptance. If x acceptance depends on $\cos\theta_e$, $\cos\theta_{av}$ is not rigorously defined, since the equality (5.7) can no longer be written. However, if the spectrum W(x) is fitted as in (5.3), with $\cos\theta_{av}$ computed from $\langle\cos\theta_\mu\cos\theta_e\rangle$ and the corrections mentioned above, then the systematic error in $r(\theta_{av})$ will be negligibly small provided that the variation in x acceptance is small for the range of $\cos\theta_e$ in the data. Therefore, in order to minimize the systematic error in $r(\theta_{av})$ due to $\cos\theta_e$-dependent x acceptance, the data were fitted in five $\cos\theta_e$ bins 0.005 wide, $0.975\leq\cos\theta_e\leq 1$. If the five $\cos\theta_e$ bins were fitted together, the systematic error in $r(\theta_{av})$ due to $\cos\theta_e$-dependent acceptance would have been $\pm 1\cdot 10^{-4}$. When each $\cos\theta_e$ bin was fitted separately, the systematic error in $r(\theta_{av})$ was smaller than $\pm 0.2\cdot 10^{-4}$

for each $\cos\theta_e$ bin. Events with $\cos\theta_e<0.975$ were dropped from analysis since they had low statistical power.

The result for $\xi P_\mu\delta/\rho$ was obtained when the five values of $r(\theta_{av})=1-(\xi P_\mu\delta/\rho)\cos\theta_{av}$, taken with asymmetric errors, were used in a fixed slope extrapolation to $\cos\theta_{av}=1$. It was checked that the result from fitting the five $\cos\theta_e$ bins separately was consistent with the result obtained when all $\cos\theta_e$ bins were fitted together.

V.C. Summary of the Analysis Method

The data were fitted separately in five $\cos\theta_e$ bins 0.005 wide, $0.975\leq\cos\theta_e\leq1$. For each $\cos\theta_e$ bin the fitting was performed in two stages. First, the spin-precessed data were fitted from x=0.93 according to (5.1). Then the resolution parameters were fixed, and the spin-held data and the spin-precessed data were fitted simultaneously, from x=0.93 and x=0.97 respectively, to determine the relative rate at the endpoint for the spin-held data, given by $r(\theta_{av})$. The spin-held data were fitted according to (5.3) and the spin-precessed data according to (5.1). For each $\cos\theta_e$ bin, $\cos\theta_{av}$ was computed from $\cos\theta_\mu\cos\theta_e$ averaged over the spin-held data, to which there were added two small corrections. Finally, the five values of $r(\theta_{av})=1-(\xi P_\mu\delta/\rho)\cos\theta_{av}$ were used in a fixed slope extrapolation to $\cos\theta_{av}=1$, which yielded $\xi P_\mu\delta/\rho$.

The analysis method was checked in two ways.

First, the positron spectra were evaluated numerically in the five $\cos\theta_e$ bins for various values of the muon decay parameters ρ, δ,

ξ and various acceptance functions $A(\theta_e,\psi_e)$ and $A(x)$. The incoming muon distribution was taken to be the measured distribution which will be discussed in section VI.B. The spectra were processed through the analysis program and the results for $r(\theta_{av})$ were compared with the prediction $[1-(\xi P_\mu\delta/\rho)\cos\theta_{av}]$, where $\cos\theta_{av}$ is defined by (5.10). It was verified that for $\tilde{\rho}=\tilde{\delta}=0$ $[\tilde{\rho}=1-(4/3)\rho,\ \tilde{\delta}=1-(4/3)\delta]$ there was always an exact agreement between $r(\theta_{av})$ and the prediction [statistical fluctuations were not introduced in the spectra]. For non-zero $\tilde{\rho}$ and $\tilde{\delta}$ the agreement was to first order in $\tilde{\rho}$ and $\tilde{\delta}$, as expected (see section II).

Second, the same analysis was applied to the data generated in the full Monte-Carlo simulation of the polarimeter. Events were generated assuming $\xi P_\mu\delta/\rho=1$. Particles were moved in small steps from the vacuum window to the stopping target for μ^+, and from the stopping target to the last wire plane in the driftchamber D4 for e^+. Scattering and energy loss were applied at each step. The data from the simulation were processed through the same event reconstruction and selection algorithm as the experimental data. After the two corrections (total of -0.00023) to $\cos\theta_{av}$ the result for $\xi P_\mu\delta/\rho$ was 0.99992 ± 0.00038, in good agreement with the expected value of 1.

V.D. Data Fitting Results

All the data were used in the analysis, with the exception of runs which had some known deficiency (e.g. too low a voltage on the driftchamber wire planes). The results for $\xi P_\mu \delta/\rho$ for all targets in the three data-taking runs (to be denoted by Run 1, etc.) are compiled in Appendix B. They are plotted in Fig. V.2, where only statistical errors are shown. The systematic errors will be considered in sections VI and VII. The results incorporate the three corrections to be discussed in section VI. One of the corrections was target-dependent, and its value for each target is also listed in Appendix B.

It was discovered during Run 2 that the thinner of the two Cu targets was not sufficiently thick to stop all muons. The amount of material beyond the mean muon stopping range is estimated to be only 2.5 straggling lengths for this target. The fitted $\xi P_\mu \delta/\rho$ for this target is significantly lower (3.0σ) than the combined result from all other targets (see Table V.1), and also lower than the combined result from the thicker Cu targets (4.6σ). Since ~0.6% of the muons which leaked out of the target could have been depolarized in air or in the mylar window of the proportional chamber P3, we have chosen not to include the result for this target in the computation of the combined result for $\xi P_\mu \delta/\rho$.

The values of $\xi P_\mu \delta/\rho$ for each metal, liquid He, and all targets together are tabulated in Table V.1 (the thinner Cu target in Run 2 is excluded; only statistical errors are listed). Let us mention

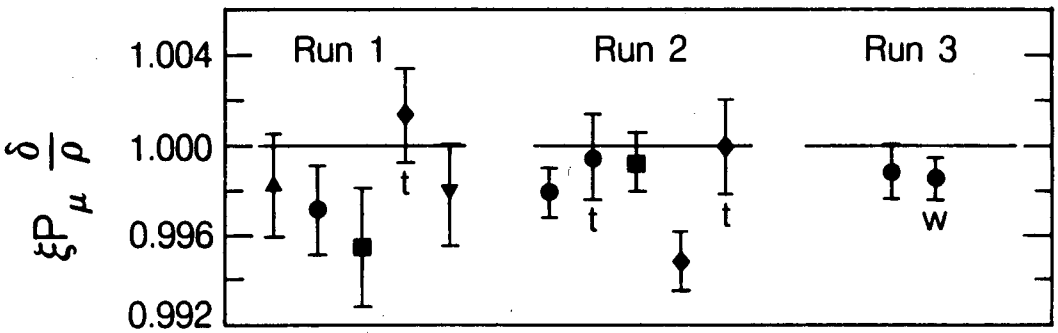

XBL 8512-11755

FIG. V.2. Results for $\xi P_\mu \delta/\rho$ for each target in the three data-taking runs (denoted by Run 1, etc.). Only statistical errors are shown. The targets are Ag (triangles), Al (circles), Au (squares), Cu (diamonds) and He (inverted triangles). The spin-holding field was 0.3 T for the target marked by "w" and 1.1 T for the other targets. The thicker targets are marked by "t". Target thicknesses are compiled in Appendix A.

TABLE V.1. Results for $\xi P_\mu \delta/\rho$ for each metal, liquid He and all targets combined. Only statistical errors are shown.

Material	$\xi P_\mu \delta/\rho$
Ag	$0.9983^{+0.0022}_{-0.0023}$
Al	$0.9985^{+0.00056}_{-0.00056}$
Au	$0.9986^{+0.0011}_{-0.0011}$
Cu	$1.0007^{+0.0015}_{-0.0015}$
He	$0.9979^{+0.0022}_{-0.0023}$
All targets	$0.9986^{+0.00046}_{-0.00046}$

here that in the analysis of the spin-precessed data using the muon spin rotation (μSR) technique[12] He was found to be 12% depolarizing. The depolarization was most likely due to muonium formation, and if so, the suppression of muon depolazation in muonium by the 1.1-T longitudinal field would explain the difference between our and μSR results. A possible reason for the muonium formation in liquid He was mentioned in section III.C.

The combined results from all targets were computed for the five $\cos\theta_e$ bins. In Fig. V.3 they are plotted as

$$\xi P_\mu \frac{\delta}{\rho} \cos\theta_{av} = 1 - r(\theta_{av})$$

versus $\cos\theta_{av}$. They incorporate the corrections to be discussed in section VI. Again, only statistical errors are shown. The fitted straight line in Fig. V.3 indicates the fixed slope extrapolation to $\cos\theta_{av}=1$.

The results for $\xi P_\mu \delta/\rho$ were also evaluated in four muon decay time ranges for the three metal targets (Al, Cu and Au) constituting 93% of the data (here the data from the thinner Cu target in Run 2 were included). The time ranges were (0.1 - 0.85) μs, (0.85 - 2.1) μs, (2.1 -5.1) μs and (5.1 - 10) μs after the muon arrival at the stopping target. As mentioned in section III.C, the stopped muon polarization is expected to decay exponentially with characteristic spin-lattice relaxation time constant T_1 toward the equilibrium situation, where the numbers of muon spins parallel or anti-parallel to the field are almost equal. If T_1 is much greater than 10 μs, the results for $\xi P_\mu \delta/\rho$ from the the four time ranges will have a linear dependence on the quantity

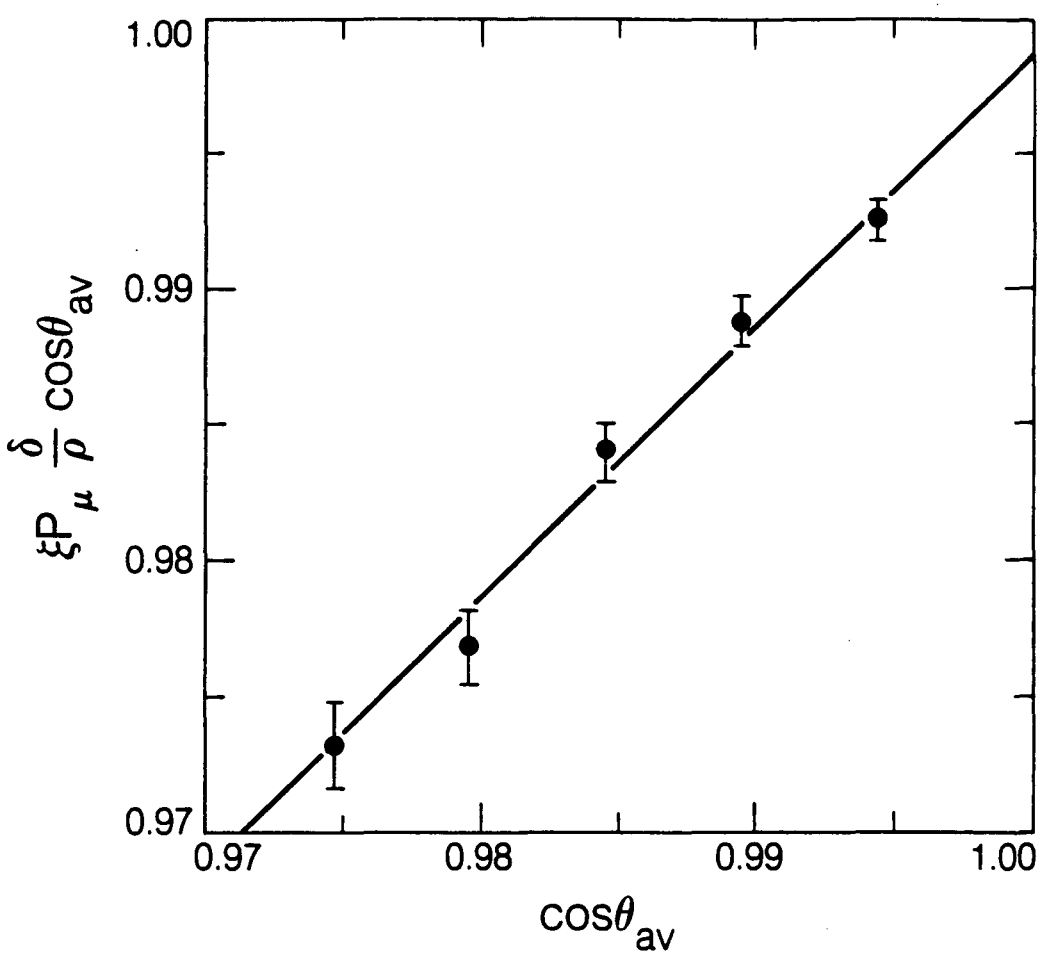

XBL 8512-11758

FIG. V.3. Results for $\xi P_\mu \frac{\delta}{\rho} \cos\theta_{av}$ from the five $\cos\theta_e$ bins plotted versus $\cos\theta_{av}$. Only statistical errors are shown. The corrections, discussed in section VI, have been incorporated. The fitted straight line indicates the fixed slope extrapolation to $\cos\theta_{av}=1$.

$$t=t_1+\tau_\mu-(t_2-t_1)\{\exp[(t_2-t_1)/\tau_\mu]-1\}^{-1} \qquad (5.12)$$

where t_1 and t_2 are the start and end of a time range.

As can be seen in Fig. V.4 only the results for Al are suggestive of a time-dependent spin relaxation. If the oscillating magnetic fields causing the spin relaxation are produced by the nuclear magnetic dipole moments, the relaxation times for Al, Cu and Au should correlate with their respective dipole moments of 3.6, 2.3 and 0.1 nuclear magnetons. The fitted slope of $(-4.3\pm3.4)\cdot10^{-4}$ μs^{-1} for Al corresponds to T_1 time of 4.6 ms, which would imply that a correction of $(+9.9\pm7.8)\cdot10^{-4}$ should be added to the result for $\xi P_\mu\delta/\rho$ for Al. Contrary to the expectation based on the result for Al, the best fit slope for Cu is actually positive $[(+4.5\pm4.8)\cdot10^{-4}$ $\mu s]$. Since our result will be used to set a lower limit on $\xi P_\mu\delta/\rho$, we have chosen a conservative approach and decided not to apply a correction due to a possible spin relaxation.

Conclusions from the result for $\xi P_\mu\delta/\rho$ will be drawn in section VIII, after we consider the corrections and systematic errors in the next two sections.

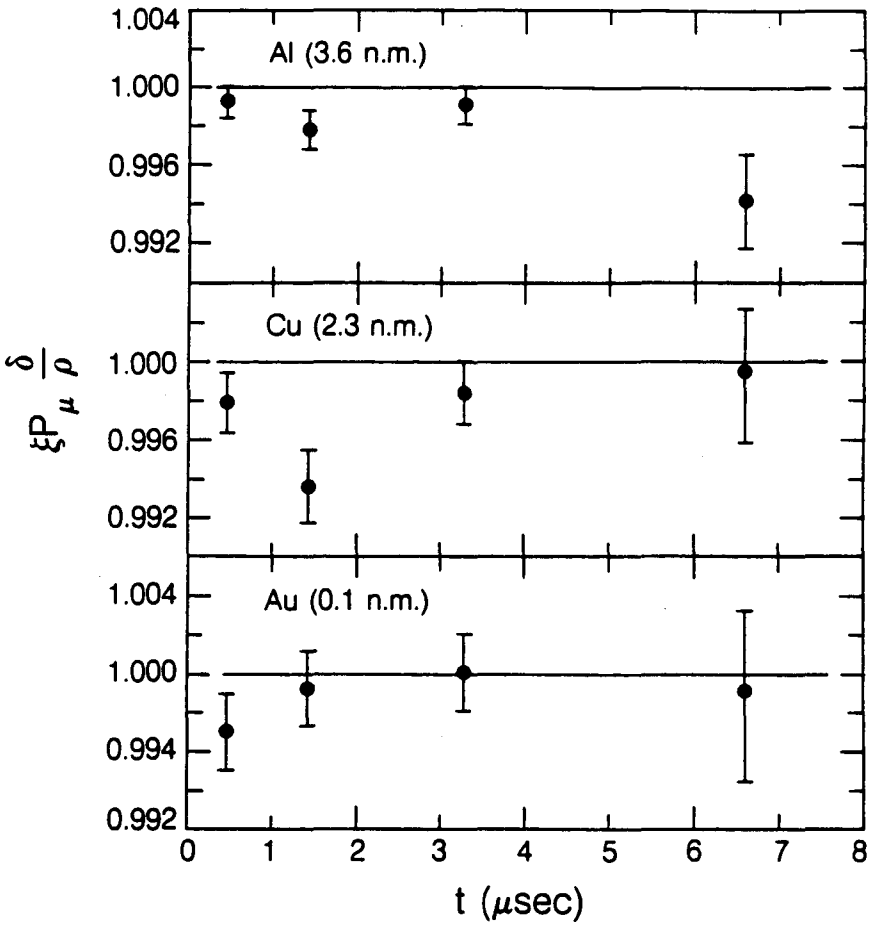

FIG. V.4. The results for $\xi P_\mu \delta/\rho$ evaluated in four muon decay time ranges for the three metal targets, Al, Cu and Au, constituting 93% of the data. Only statistical errors are shown. The results are plotted versus t, given by equation (5.12). The target material nuclear magnetic moment in units of nuclear magnetons (n.m.) is indicated. Only the results for Al are suggestive of a time-dependent spin relaxation.

VI. CORRECTIONS

This chapter describes the computation of three corrections. Two corrections were applied to $\cos\theta_{av}$, computed from data-averaged $\cos\theta_\mu\cos\theta_e$. Another correction was applied to the result for $\xi P_\mu\delta/\rho$ due to muon depolarization during the stopping process in scattering with unpolarized electrons. The reasons for these corrections have been mentioned in section V.B. We will continue to use the notation introduced in that section.

Let us briefly repeat the reasons for the corrections to $\cos\theta_{av}$. In the expression (5.4) for the rate at the endpoint $\cos\theta_{av}$ is defined by (5.10). However, in the analysis $\cos\theta_{av}$ had to be computed from $\langle\cos\theta_\mu\cos\theta_e\rangle$, i.e. $\cos\theta_\mu\cos\theta_e$ averaged over the spin-held data. Two corrections had to be added to $\langle\cos\theta_\mu\cos\theta_e\rangle$. The first correction was due to the difference between $\langle\cos\theta_\mu\cos\theta_e\rangle$ computed from the measured tracks, and $\langle\cos\theta_\mu\cos\theta_e\rangle$ if it were computed from the true values of θ_μ and θ_e. This correction was mostly due to multiple scattering, although finite chamber resolution also contributed. Since positron scattering depended on the target, this correction was target dependent. The second correction was due to the difference between $\langle\cos\theta_\mu\cos\theta_e\rangle$, given by (5.11), and $\cos\theta_{av}$ defined by (5.10).

The values of the three corrections and the uncertainties in them are listed in Table VI.1. It should be noted that adding a correction to $\cos\theta_{av}$, i.e. to $\langle\cos\theta_\mu\cos\theta_e\rangle$, was equivalent to reducing $\xi P_\mu\delta/\rho$ by the same amount because $\langle\cos\theta_\mu\cos\theta_e\rangle$ was nearly 1.

TABLE VI.1. Values of corrections to $\cos\theta_{av}$ and $\xi P_\mu \delta/\rho$ and estimated possible systematic errors in corrections. Adding a correction to $\cos\theta_{av}$ is equivalent to reducing $\xi P_\mu \delta/\rho$ by the same amount.

Corrections	Values	Errors
Correction to $\xi P_\mu \delta/\rho$ due to muon depolarization in scattering with unpolarized electrons	+0.0007	<0.0001
Correction (averaged over all targets) to $\cos\theta_{av}$ due to Coulomb scattering and finite chamber resolution	-0.0001	±0.0003
Correction to $\cos\theta_{av}$ due to use of data averaged $\cos\theta_\mu \cos\theta_e$	+0.0001	<0.0001

The possible systematic errors in two of the three corrections listed in Table VI.1 are estimated to be small compared to $1 \cdot 10^{-4}$.

The three corrections will be considered below in this order: first, the correction to $\cos\theta_{av}$ due to multiple scattering and finite chamber resolution; second, the correction to $\cos\theta_{av}$ due to use of (5.11), rather than (5.10); finally, the correction to $\xi P_\mu \delta/\rho$ due to muon depolarization in scattering with unpolarized electrons.

VI.A. Correction due to Multiple Scattering and Finite Chamber Resolution

Let us denote $\langle\cos\theta_\mu \cos\theta_e\rangle$ computed from the measured tracks by $\langle\cos\theta_{meas}\rangle$, and $\langle\cos\theta_\mu \cos\theta_e\rangle$ if it were computed from the true values of θ_μ and θ_e by $\langle\cos\theta_{true}\rangle$. The unit vector given by the extrapolation of the measured muon track to the stopping target will be denoted by $\hat{p}_{\mu,meas}$, and $\theta_{\mu,meas}$ will denote the corresponding polar angle with respect to the solenoid axis. $\theta_{\mu,true}$ will denote the true polar angle of $-\hat{s}_\mu$ at the decay vertex.

Muon depolarization due to scattering with unpolarized electrons, which is considered in section VI.C, will be ignored. Coulomb scattering is relativistically helicity conserving and non-relativistically spin-conserving. The non-relativistic limit applies to the μ^+, which initially have β=0.27 (when a muon with helicity ± 1 scatters by an angle θ, muon polarization with respect to the initial direction changes by $\approx\theta^2\beta^4/8$). It can therefore be assumed that the spin polar angle θ_μ, when a muon enters the stopping

target, is identical to $\theta_{\mu,true}$. The true direction of muon spin when the muon enters the stopping target will be denoted by $\hat{s}_{\mu,ent}$. Similarly, let $\hat{p}_{e,true}$ denote the direction of e^+ momentum at the decay vertex, and $\theta_{e,true}$ the corresponding polar angle. Let the unit vector given by the extrapolation of the measured positron track to the stopping target be denoted by $\hat{p}_{e,meas}$, and $\theta_{e,meas}$ be the corresponding polar angle.

We seek the correction $\langle\cos\theta_{true}\rangle-\langle\cos\theta_{meas}\rangle$. Since $\cos\theta_\mu$ and $\cos\theta_e$ are both very close to 1,

$$\cos\theta_\mu\cos\theta_e\approx\cos\theta_\mu+\cos\theta_e-1 \ ,$$

and hence

$$\langle\cos\theta_{true}\rangle-\langle\cos\theta_{meas}\rangle\approx[\langle\cos\theta_{\mu,true}\rangle-\langle\cos\theta_{\mu,meas}\rangle] + [\langle\cos\theta_{e,true}\rangle-\langle\cos\theta_{e,meas}\rangle] \ . \tag{6.1}$$

Let us consider qualitatively various contributions to the muon average in (6.1), i.e. to the first term on the right-hand side. Similar arguments will apply for positrons. There are several sources of misalignment between $\hat{s}_{\mu,ent}$ and $\hat{p}_{\mu,meas}$. Before the muon enters the vacuum window separating the beamline from the muon polarimeter (it is located just in front of the proportional chamber P1; see Fig. III.1), $\hat{s}_\mu$ and $\hat{p}_\mu$ are misaligned due to scattering in the production target. Muon scattering in the material (~50 mg/cm^2) upstream of the stopping target contributes further to the misalignment. Although scattering of the muons is assumed to be spin-conserving, the muon spin direction does change between the vacuum window and the stopping target due to spin precession in the longitudinal field.

In order to estimate the effects of muon scattering in the production target and in the material upstream of the stopping target, let us ignore the magnetic field in the stopping target region. It can therefore be assumed that muon spin direction does not change when a muon travels from the vacuum window to the stopping target. Let us denote the true direction of the muon momentum before the muon enters the P1 vacuum window by $\hat{p}_i$ (subscript i stands for 'initial'). Let θ_i be the corresponding polar angle. The muon average in (6.1) can be rewritten as

$$[\langle\cos\theta_{\mu,true}\rangle-\langle\cos\theta_i\rangle] + [\langle\cos\theta_i\rangle-\langle\cos\theta_{\mu,meas}\rangle]. \qquad (6.2)$$

Without a loss of generality, we may assume that at the π^+ decay vertex $\hat{s}_\mu$ is always anti-parallel to $\hat{p}_\mu$. Let us consider the first term in (6.2). The misalignment between $\hat{s}_{\mu,ent}$ (which determines $\cos\theta_{\mu,true}$ since the magnetic field is ignored) and $\hat{p}_i$ is due to scattering in the production target. For simplicity, let the scattering angle ϕ_1 in the production target be the same for all muons. The angle ϕ_1 between $\hat{s}_\mu$ and $\hat{p}_\mu$ is preserved by the magnetic field in the beamline, where muons are transported in vacuum. At the vacuum window $\hat{s}_\mu$ is randomly misaligned with respect to $\hat{p}_i$ by an angle ϕ_1. By a simple computation

$$\langle\cos\theta_{\mu,true}\rangle=\langle\cos\theta_i\rangle\cos\phi_1 \ , \qquad (6.3)$$

and since ϕ_1 is small (~30 mrad) and $\cos\theta_i\approx1$,

$$[\langle\cos\theta_{\mu,true}\rangle-\langle\cos\theta_i\rangle]\approx-\phi_1{}^2/2 \ . \qquad (6.4)$$

Let us now consider the second term in (6.2). The misalignment between $\hat{p}_i$ and $\hat{p}_{\mu,meas}$ is mostly due to scattering between the vacuum window and the proportional chamber P2, although finite chamber

resolution and finite accuracy of track extrapolation also contribute. To a good approximation, only material upstream of the mid-point between P1 and P2 contributes to the misalignment ($5\cdot10^{-4}$ radiation lengths). The acceptance effects and software cuts preferentially reject events with the largest μ^+ scattering angles between the vacuum window and P2, which leads to a decrease ($\sim6\cdot10^{-4}$) in the correction. We will return to these effects below, when we consider the systematic errors in the correction, but for the moment suppose that these effects can be ignored. Again, let the angle ϕ_2 between $\hat{p}_i$ and $\hat{p}_{\mu,meas}$ be the same for all muons. The unit vectors $\hat{p}_{\mu,meas}$ are randomly misaligned with respect to p_i by an angle ϕ_2. Hence

$$\langle\cos\theta_{\mu,meas}\rangle=\langle\cos\theta_i\rangle\cos\phi_2$$

by the same computation as in (6.3), and

$$[\langle\cos\theta_i\rangle-\langle\cos\theta_{\mu,meas}\rangle]\approx\phi_2{}^2/2 \ . \qquad (6.5)$$

Therefore the correction for μ^+ scattering in the material near the stopping target, given by (6.5), has an opposite sign from the correction for μ^+ scattering in the production target, given by (6.4).

Since the correction (6.1) depends on the geometrical acceptance of the apparatus, on cuts in analysis, on angular distribution of the incoming muons, etc., it is not possible to compute it precisely by an analytical computation. Furthermore, the positron average in (6.1) depends on the target so that the correction is also target-dependent. The corrections were therefore computed, to a statistical error of less than $\pm0.5\cdot10^{-4}$ for each stopping target, in a full Monte-Carlo simulation of the polarimeter described in section

V.C. The scattering model used in the simulation is based on the theory of Nigam, Sundaresan and Wu.[32] The data generated in the simulation were processed through the same event reconstruction and selection algorithm as the experimental data, and the correction (6.1) was computed from Monte-Carlo events which passed all cuts. The correction varied by less than $2.5 \cdot 10^{-4}$ from $\cos\theta_e = 0.975$ to $\cos\theta_e = 1$ for all targets. Hence, the correction was assumed to be the same for all $\cos\theta_e$ bins, since it was found that the error in $\xi P_\mu \delta/\rho$ due to this assumption was less than $\pm 0.5 \cdot 10^{-4}$. The corrections for all targets are tabulated in Appendix B. They include an upward adjustment of $2 \cdot 10^{-4}$ discussed below.

Let us now consider the possible systematic errors in the correction (6.1). The accuracy of the scattering model, assumed to be ±10% in the scattering angle magnitude, leads to an error of $< 1 \cdot 10^{-4}$, but conservatively it is taken to be $\pm 1 \cdot 10^{-4}$. As can be seen from equations (6.4) and (6.5), the value of the correction should vary quadratically with the scattering angle magnitude if acceptance effects can be ignored. This quadratic dependence approximately holds in practice. The error due to the uncertainty in the scattering angle magnitude is relatively small because the correction for muon scattering in the production target has an opposite sign from the correction due to scattering near the stopping target: the muon part of the correction (6.1) is $0.1 \cdot 10^{-4}$ (total), compared to the contribution of scattering in the production target of $-4 \cdot 10^{-4}$. The positron part of the correction, averaged over the stopping targets, is $-1 \cdot 10^{-4}$.

The correction (6.1) depends on the fraction of events with large scattering angles remaining in the final sample. The number of such events in the final sample is reduced because of software cuts requiring $\cos\theta_\mu \geq 0.99$ and a radius at the stopping target ≤ 1.8 cm. Also, such events have a larger beam spot at the stopping target, and consequently there is a smaller probability for a positron to be accepted by the apparatus. The correction (6.1) therefore depends on the distribution of incoming μ^+ angles, and to a smaller extent on the beam spot at the target.

The true muon distribution in angles and position at the P1 vacuum window is not known since the measured distribution includes the effects of scattering. Let us explain how the measured distribution was obtained. In the experiment, when the data was collected in the spin-precessing mode (i.e. with 70-G or 110-G vertical field), approximately every thirtieth event was taken with a 'μ-stop' trigger, requiring only a signature of a particle stopping in the target. The angular distribution of the measured muon tracks in such events was used in the Monte-Carlo simulation.

Since essentially all muons at the P1 vacuum window are accepted by the apparatus, it is possible to estimate the true μ^+ distribution that would yield the measured distribution. When the estimated true μ^+ distribution was used to compute the correction, the muon part of the correction was $\approx 2\cdot 10^{-4}$ greater then it was with the measured distribution. Therefore, all corrections computed with the measured distribution were adjusted upwards by $2\cdot 10^{-4}$, and a possible systematic error of $\pm 2\cdot 10^{-4}$ was assigned to the correction (6.1) due

to the uncertainty in the incoming μ^+ distribution.

Finally, the correction (6.1) depends on the amount of scattering in the production target. The mean thickness of material in the production target traversed by muons is determined by the mean beam momentum, estimated to be 29.45 MeV/c. The μ^+ momentum from π^+ decay at rest is 29.79 MeV/c, which implies that the mean energy loss in the graphite production target was 0.0092 MeV, corresponding to a mean thickness traversed by muons of 6.6 mg/cm^2. An uncertainty in the mean μ^+ beam momentum of ±0.2 MeV/c implies an uncertainty of 3.8 mg/cm^2 in the mean thickness traversed by muons, which leads to a possible systematic error in the correction of $\pm 2 \cdot 10^{-4}$.

When these three systematic errors are added in quadrature, the combined possible systematic error in the correction (6.1) becomes $\pm 3 \cdot 10^{-4}$. The correction averaged over all targets was $-1 \cdot 10^{-4}$.

VI.B. Correction due to Use of Data-Averaged $\cos\theta_\mu\cos\theta_e$

We seek a correction due to the difference between $\cos\theta_{av}$ defined by (5.10), and the data-averaged $\cos\theta_\mu\cos\theta_e$ given by (5.11). The latter will be denoted by $\langle\cos\theta_\mu\cos\theta_e\rangle$, just as before. The correction required is given by

$$\cos\theta_{av}-\langle\cos\theta_\mu\cos\theta_e\rangle \ . \tag{6.6}$$

Here it is assumed that $\langle\cos\theta_\mu\cos\theta_e\rangle$ has been computed from the true values of θ_μ and θ_e.

In section V.B it was shown that when statistical fluctuations are ignored, the positron spectrum for the fitted subset of the spin-held data is given by

$$W(x) \sim \int[a(x)+b(x)\xi P_\mu\cos\theta]A(\theta_e,\psi_e)A(x)R(\theta_\mu)d\omega_e d\omega_\mu \tag{6.7}$$

where a(x) and b(x) are the angle-dependent and angle-independent parts of the muon decay rate; $A(\theta_e,\psi_e)$ is the angular acceptance function for positrons, assumed to be independent of the x acceptance function A(x); $R(\theta_\mu)$ denotes the θ_μ distribution of muon spins at the decay vertex for muons reaching the stopping target (the distribution is isotropic in ψ_μ); $d\omega$ denotes the integration over the angular phase space, i.e. $d\omega_e=d(\cos\theta_e)d\psi_e$; and

$$\cos\theta=\cos\theta_\mu\cos\theta_e+\sin\theta_\mu\sin\theta_e\cos\psi_\mu\cos\psi_e+\sin\theta_\mu\sin\theta_e\sin\psi_\mu\sin\psi_e \ .$$

The two terms in the expression for $\cos\theta$ which contain ψ_μ, vanish in (6.7) after integration. Aside from $\cos\theta$, only $A(\theta_e,\psi_e)$ in (6.7) depends on ψ_e. Hence, W(x) can be rewritten in terms of the angular acceptance function which depends only on θ_e:

$$A(\theta_e)=\int A(\theta_e,\psi_e)d\psi_e \ . \tag{6.8}$$

This fact will be useful for the discussion below.

The correction (6.6) depends on the range of $\cos\theta_e$ in the fitted data set, and also on the minimum x in the fit of the spin-held data. For $\cos\theta_e$ bins 0.005 wide and x_{min}=0.97, the correction was small, only $+1\cdot10^{-4}$, and to an accuracy of $\pm0.1\cdot10^{-4}$ it was the same for all $\cos\theta_e$ bins. The correction was computed by evaluating the spectrum W(x) numerically, using the estimated true $R(\theta_\mu)$ distribution (see section VI.A), and assuming that A(x) and $A(\theta_e,\psi_e)$ were constant.

It was checked that the correction changed negligibly for realistic A(x) and $A(\theta_e)$. The x acceptance varied the most in the smallest $\cos\theta_e$ bin (i.e. $0.975\leq\cos\theta_e<0.98$ bin). When the spin-precessed data were combined from all targets and fitted according to (5.1), with A(x) given by (5.2), it was found that the x acceptance in this $\cos\theta_e$ bin fell by 17% at x=.93 and by 1.5% at x=1, relative to the acceptance maximum at x=0.985. The correction (6.6) changed by less than $0.1\cdot10^{-4}$ when this A(x) was used in the computation of W(x).

The angular acceptance $A(\theta_e)$ for the spin-held data should be similar to $A(\theta_e)$ for the spin-precessed data. The latter is given by the number of events as a function of $\cos\theta_e$, since after timing cuts the spin-precessed data is equivalent to the unpolarized, i.e. P_μ=0, data, and the angular distribution of decay positrons for P_μ=0 data is isotropic. The angular acceptance at $\cos\theta_e$=0.975 fell by ~20% relative to $\cos\theta_e$=1. The correction (6.6) changed by less than $0.1\cdot10^{-4}$ for a 10% variation in $A(\theta_e)$ in a single $\cos\theta_e$ bin.

Since $A(\theta_e)$ depends on x, one may define $\cos\theta_{av}$ using the angular acceptance function for the center of the fitted $\cos\theta_e$ bin. If such acceptance function is denoted by $A_c(\theta_e)$, then

$$\cos\theta_{av} = \frac{\int \cos\theta_\mu \cos\theta_e A_c(\theta_e) R(\theta_\mu) d(\cos\theta_e) d\omega_\mu}{\int A_c(\theta_e) R(\theta_\mu) d(\cos\theta_e) d\omega_\mu} .$$

With this definition of $\cos\theta_{av}$ the correction (6.6) is still accurate to $\pm 0.1 \cdot 10^{-4}$ for a realistic variation of $A(\theta_e)$ with x.

VI.C. Muon Depolarization in Scattering with Unpolarized Electrons

Let us denote by the unit vector $\hat{\sigma}_\mu$ the direction the muon spin would have if scattering with electrons were absent. Muon polarization with respect to $\hat{\sigma}_\mu$ is reduced due to spin-exchange effects in scattering with unpolarized electrons. The polarization with respect to $\hat{\sigma}_\mu$ would have been preserved in the absence of scattering. For simplicity, let us assume that at the π^+ decay vertex the muon spin is anti-parallel to $\hat{p}_\mu$, as it is for a pure V-A interaction. Let the solenoid axis define the z-direction. Muon depolarization with respect to $\hat{\sigma}_\mu$ in scattering with unpolarized electrons during the stopping process will be denoted by ΔP. We will continue to assume that Coulomb scattering from nuclei is spin-conserving. The expectation value of the muon spin $\hat{s}_\mu$ with respect to $\hat{\sigma}_\mu$ is

$$\langle \hat{s}_\mu \rangle_{\hat{\sigma}_\mu} = (\hbar/2)(1-\Delta P) ,$$

which implies that the expectation value with respect to the z-axis is

$$\langle \hat{s}_\mu \rangle_z = (1-\Delta P)\ \langle \hat{\sigma}_\mu \rangle_z \ .$$

In section VI.A the correction (6.1), due to the difference between $\langle \cos\theta_\mu \cos\theta_e \rangle$ computed from the measured tracks and $\langle \cos\theta_\mu \cos\theta_e \rangle$ computed from the true values of θ_μ and θ_e, has been found assuming that $\cos\theta_{\mu,true}$ is given by the z-component of $\hat{\sigma}_\mu$, rather than by $\langle \hat{s}_\mu \rangle_z$. Hence, after the correction (6.1) has been added to $\langle \cos\theta_\mu \cos\theta_e \rangle$, the resulting value must in addition be multiplied by $(1-\Delta P)$. Since ΔP is only $7\cdot 10^{-4}$, as will be shown below, and $\langle \cos\theta_\mu \cos\theta_e \rangle$ is >0.97, an upward correction equal to ΔP has been made directly to the result for $\xi P_\mu \delta/\rho$.

We now consider the computation of ΔP. It was shown by Ford and Mullin[28] that for a non-relativistic μ^+ which scatters with unpolarized e^- through a center of mass angle θ, the probability that the final μ^+ spin direction is parallel ($\varepsilon=1$) or anti-parallel ($\varepsilon=-1$) to the initial spin is

$$Q(\varepsilon,\theta) = \frac{1+\varepsilon}{2} - \varepsilon \frac{m^2}{\mu^2} \beta^4 \left[\sin^2(\theta/2) - \sin^4(\theta/2) + \sin^6(\theta/2)\right]$$

where β is the muon velocity in the lab frame and $m=m_e$ and $\mu=m_\mu$. If the muons are initially fully polarized, the polarization along the direction $\hat{\sigma}_\mu$ after one scatter is

$$P_\mu = 1 - 2 \frac{m^2}{\mu^2} \beta^4 \left[\sin^2(\theta/2) - \sin^4(\theta/2) + \sin^6(\theta/2)\right]\}$$

and similarly, if the polarization is initially $P_{\mu,i}$, the polarization $P_{\mu,f}$ after one additional scatter is

$$P_{\mu,f} = P_{\mu,i}\{1 - 2\frac{m^2}{\mu^2}\beta^4\,[\sin^2(\theta/2) - \sin^4(\theta/2) + \sin^6(\theta/2)]\}.$$

The corresponding fractional energy loss is

$$w = \frac{m}{\mu}\beta^2\sin^2(\theta/2)\ .$$

One can write a differential equation for the depolarization as a function of energy. For the energy loss $dE = wE$, where E is the muon kinetic energy $E = (\gamma-1)\mu$, the rate of depolarization is

$$\frac{dP_\mu}{dE} = P_\mu(E)\ \{\ 2\frac{m}{\mu^2}\frac{\beta^2}{(\gamma-1)}\,[1 - \sin^2(\theta/2) + \sin^4(\theta/2)]\}\ . \qquad (6.7)$$

The non-relativistic cross-section is inversely proportional to $\sin^4(\theta/2)$, and hence the $\sin(\theta/2)$ terms in (6.7) can be ignored. The polarization $P_\mu(E)$ will be >.999, and can be set equal to unity on the right-hand side. Surface muons, coming from π^+ decay at rest, initially have kinetic energy E_0=4.1 MeV. Since muon energy loss for E>3 KeV is almost entirely due to scattering with electrons (see section III.C), ΔP is given by

$$\Delta P = \int_{3\ \mathrm{keV}}^{E_0} 2\frac{m}{\mu^2}\frac{\beta^2}{(\gamma-1)}\,dE \approx 2\frac{m}{\mu^2}\int_0^{E_0}[2 - 3\frac{E}{\mu}]\,dE \approx$$

$$\approx 4\frac{mE_0}{\mu^2}(1 - \frac{3}{4}\frac{E_0}{\mu}) \approx 7.3\cdot 10^{-4}.$$

It should be noted that ΔP is relativily insensitive to the lower limit in the integration. The uncertainty in this correction is therefore estimated to be small compared to 10^{-4}.

The values of all corrections and the uncertainties in them have been listed in Table VI.1.

VII. SYSTEMATIC ERRORS

The possible sources of systematic errors $\geq 1 \cdot 10^{-4}$ are summarized in Table VII.1. The systematic error in the scattering correction has been discussed in section VI.A. The sources of the remaining systematic errors will be considered one at a time below. The systematic errors listed in Table VII.1 should in principle be uncorrelated; they add in quadrature to $\pm 7.5 \cdot 10^{-4}$.

At the end of this section we will also consider the systematic error due to events with decay positrons produced by an extra muon in the stopping target, rather than the muon causing the trigger. This error will be shown to be small compared to $1 \cdot 10^{-4}$.

VII.A. x=1 Calibration

Recall that the x=1 calibration was determined from the x=1 edge position in the spin-precessed data (see section V.A). The position of the x=1 point on the reconstructed momentum scale was a free parameter in the first stage of fitting, when the spin-precessed data were fitted alone, and in the second stage, when the spin-held and spin-precessed data were fitted simultaneously. The position of x=1 was assumed to be identical for the two data sets. However, the x=1 calibration points may differ because of the strong longitudinal field in the target region for the spin-held data, which provided extra bending for positron trajectories. Hence, for the same x, positron trajectories in the two data sets had a different

TABLE VII.1. The possible sources of systematic error $\geq 1 \cdot 10^{-4}$ and their estimated contributions.

Sources of Possible Error	Errors
Coulomb scattering correction	±0.0003
Difference in x=1 calibration (±.00035) and x acceptance (±.0002) between the spin-held and spin-precessed data	±0.00055
Spectrometer momentum dispersion	±0.0001
Uncertainty in the longitudinal position of wire planes for chambers near the target	±0.00025
Accuracy of $\cos\theta_\mu$ and $\cos\theta_e$ reconstruction using first-order optics approximation	±0.00025
Total 1σ possible error	±0.00075

distribution in the spectrometer magnet, and there could be a small difference in x=1 calibration points due to imperfections in the momentum reconstruction algorithm. Let us denote by $x_{1,s-h}$ the position of x=1 for the spin-held data. Similarly, let $x_{1,s-p}$ denote the position of x=1 for the spin-precessed data.

The possible difference in x=1 calibration

$$\Delta x_1 = x_{1,s-h} - x_{1,s-p}$$

was estimated by fitting the data. We have chosen not to rely on the results from the Monte-Carlo simulation, since the simulation did not use the measured spectrometer field. The field in the simulation was computed assuming a cylindrical symmetry and hence it was only approximate.

The position of x=1 for the spin-precessed data, i.e. $x_{1,s-p}$, was already known from the first stage of fitting. The position of x=1 for the spin-held data, i.e. $x_{1,s-h}$, was determined by fitting the spin-held data according to (5.3), just as before, but leaving the position of x=1 as a free parameter. In order to increase the statistical power of the spin-held data to determine the position of x=1, the cut to eliminate cloud muons (described in section III.B) was not applied.

The mean Δx_1 averaged over all five $\cos\theta_e$ bins and all targets was found to be $(0.17\pm0.45)\cdot10^{-4}$ (χ^2=36 for 54 degrees of freedom). The slope in Δx_1 versus $\cos\theta_e$ was consistent with zero (0.0010 ± 0.0066), and hence Δx_1 was assumed to be the same for all $\cos\theta_e$ bins. It was found empirically that for a non-zero Δx_1 the error in $\xi P_\mu \delta/\rho$ was $8\Delta x_1$. This error was determined by shifting the

spin-held data in x and observing the resulting change in $\xi P_\mu \delta/\rho$. Since our result will be used to set a lower limit on $\xi P_\mu \delta/\rho$, a conservative approach was chosen and an upwards correction to $\xi P_\mu \delta/\rho$ due to a positive central value of Δx_1 was not made. Hence, just a systematic error of $\pm 3.5 \cdot 10^{-4}$ was assigned to $\xi P_\mu \delta/\rho$.

VII.B. Momentum acceptance

The acceptance in reduced positron momentum x, which was assumed to be the same for the spin-held and spin-precessed data, may also differ because of the strong longitudinal field in the target region. Let us introduce a function D(x) to describe the possible difference in x acceptance between the two data sets. Since the normalization was a free parameter in the fit, it may be assumed that D(1)=1. The lowest order, i.e. linear, term in D(x) may be estimated by extending the minimum x for the spin-held data from x=0.97 down to x=0.93, and adding D(x) to the fitting function for the spin-held data (5.3). The fitting function for the spin-held data then becomes

$$N_2\{[1-r(\theta_{av})]S_{V-A}(x,1) + r(\theta_{av})S_{V-A}(x,0)\}A(x)D(x)$$

where N_2 is a free normalization; $S_{V-A}(x,1)$ and $S_{V-A}(x,0)$ are the pure V-A spectra at $P_\mu \cos\theta=1$ and $P_\mu \cos\theta=0$ respectively; $r(\theta_{av})$ is the relative rate at the end-point; A(x) is the quadratic acceptance function (5.2); and D(x) describes the difference in acceptance between the spin-held and spin-precessed data:

$$D(x) = 1 + D_1(x-1)$$

where D_1 is a free parameter.

The mean D_1, averaged over the five $\cos\theta_e$ bins and all targets, was found to be 0.14±0.18 (χ^2=44 for 54 degrees of freedom). The slope in D_1 versus $\cos\theta_e$ was consistent with zero (7±27), and hence D_1 was assumed to be the same for all $\cos\theta_e$ bins. It was empirically determined that when D(x) was used in the fit of the spin-held data, the result for $\xi P_\mu \delta/\rho$ changed by $0.001 \cdot D_1$ relative to its value with D_1=0. The rate of change in $\xi P_\mu \delta/\rho$ with D_1 varied quadratically with $(1-x_{min})$, where x_{min} is the minimum x in the fit of the spin-held data. The x_{min} of 0.97 was optimal for the smallest combined (statistical and systematic) error.

A conservative approach was chosen here, just as for the x=1 calibration error, and an upward correction to $\xi P_\mu \delta/\rho$ due to a positive central value of D_1 was not made. A systematic error of $\pm 2 \cdot 10^{-4}$ was assigned to $\xi P_\mu \delta/\rho$ due to a possible difference in x acceptance between the spin-held and spin-precessed data.

Since the possible differences in the x=1 calibration and x acceptance are both due to the longitudinal field in the target region, these two errors were combined linearly in the computation of the total systematic error.

VII.C. Momentum Dispersion

The spectrometer momentum dispersion was measured to be (1.056±0.008)%/cm (see section IV). Let us estimate the change in $\xi P_\mu \delta/\rho$ if the dispersion is decreased, for example. A decrease in the dispersion means that the reconstructed reduced positron momentum x is shifted closer to x=1. Hence one may think of the change in dispersion in terms of a factor λ ($\lambda<1$) by which the reconstructed momentum scale is compressed towards x=1.

The spin-held data is given approximately by a linear function vanishing at x=1 plus a constant. It can be therefore easily shown that when the x scale is compressed by a factor λ, the normalization parameter N_2 in the fitting function for the spin-held data (equation 5.3) increases by a factor of $\approx 1/\lambda^2$. Near x=1 the number of events per x bin increases by a factor of $1/\lambda$. Since this number is proportional to $N_2 r(\theta_{av})$, where $r(\theta_{av})$ is the relative rate at the end-point, $r(\theta_{av})$ decreases by a factor of λ, as was verified in the analysis. Recall that $\xi P_\mu \delta/\rho$ was extracted from $r(\theta_{av})=1-(\xi P_\mu \delta/\rho)\cos\theta_{av}$. The mean $r(\theta_{av})$ was 0.015, and hence a possible systematic error of $\pm 1\cdot 10^{-4}$ was assigned to $\xi P_\mu \delta/\rho$ due to an uncertainty in the spectrometer momentum dispersion.

VII.D. Reconstruction of $\cos\theta_\mu$ and $\cos\theta_e$

There are two more sources of possible systematic errors in the reconstruction of $\cos\theta_\mu$ and $\cos\theta_e$, in addition to the systematic error in the scattering correction to $\langle\cos\theta_\mu\cos\theta_e\rangle$, which was discussed in section VI.A. Here we will first consider the systematic errors due to the uncertainties in the longitudinal positions of the wire planes in the proportional chambers near the target. Then we will consider a systematic error due to fitting curved tracks in the first-order optics approximation for cylindrically symmetric fields, described in section IV.

Let us denote the difference between $\langle\cos\theta_\mu\rangle$ (i.e. the data-averaged $\cos\theta_\mu$) if it were computed from the true angles and $\langle\cos\theta_\mu\rangle$ computed from the measured angles by $\Delta\cos\theta_\mu$. Similarly, $\Delta\cos\theta_e$ will denote the difference for positrons. An uncertainty of ±2 mm in the longitudinal distance between the proportional chambers P1 and P2 (see Fig. III.1) leads to a systematic error of $\pm 2\cdot 10^{-4}$ in $\Delta\cos\theta_\mu$, and consequently in $\xi P_\mu \delta/\rho$. An uncertainty of ±2 mm in the longitudinal position of the proportional chamber P3 with respect to the drift chambers D1 and D2 leads to a systematic error of $\pm 1.5\cdot 10^{-4}$ in $\Delta\cos\theta_e$. These errors are combined in quadrature to yield $\pm 2.5\cdot 10^{-4}$.

In the first-order optics approximation particle trajectories are determined by means of transfer matrices, computed from the magnetic field values on the solenoid axis and the magnetic rigidity. In the region from the proportional chamber P1 to the driftchamber D2 the

magnetic field is given by the sum of the 'upstream' field, produced by the two coils surrounding the target, and the 'downstream' field, produced by the coils in the solenoid bore. The two sets of coils were powered independently.

In track reconstruction we have used the axial field computed by the POISSON program. A comparison was made between the POISSON axial field and the measured axial field (the measurements were taken at different magnet currents than those used in the experiment). For the comparison the upstream POISSON field was scaled so that there was an agreement in the axial field at the target, and the downstream POISSON field was scaled to obtain agreement in the axial field at the last wire plane in driftchamber D2. After the normalization, the POISSON axial field agreed with the measured field to within 12%. The measured field was always lower than the POISSON field, with the largest difference being near the field minimum in driftchamber D1 and in the upstream field tail near P1.

The optimal scaling factors for the upstream and downstream fields for track reconstruction were determined by minimizing the average χ^2 for the curved positron tracks. When the scaling factors were determined in an identical manner for the data from the full Monte-Carlo simulation of the polarimeter, it was found that in the absence of scattering and chamber resolution effects $\Delta\cos\theta_\mu$ was $+2\cdot10^{-6}$ and $\Delta\cos\theta_e$ was $-2\cdot10^{-5}$. Hence, the accuracy of the first-order optics approximation in determining $\cos\theta_\mu$ and $\cos\theta_e$ is assumed to be less than $\pm1\cdot10^{-4}$. The systematic errors in $\Delta\cos\theta_\mu$ and $\Delta\cos\theta_e$ are assigned due to the uncertainties in determining the

scaling factors, and due to the difference between the POISSON and measured axial fields.

The scaling factors were determined to an accuracy of less than 5%. To allow for the difference between the POISSON and measured axial fields, the systematic errors in $\Delta\cos\theta_\mu$ and $\Delta\cos\theta_e$ are assumed conservatively to correspond to a 10% change in the scaling factors. For a 10% change in the scaling factor for the upstream field, $\Delta\cos\theta_\mu$ changed by $8\cdot10^{-5}$ and $\Delta\cos\theta_e$ by $5\cdot10^{-5}$. For a 10% change in the scaling factor for the downstream field, $\Delta\cos\theta_e$ changed by $1\cdot10^{-4}$. Hence a possible systematic error of $2.5\cdot10^{-4}$ is assigned to $\xi P_\mu\delta/\rho$ due to an uncertainty in the accuracy of $\cos\theta_\mu$ and $\cos\theta_e$ reconstruction using the first-order optics approximation.

VI.D. Extra Muons

A small fraction of events in the final sample have decay positrons produced by an extra muon in the stopping target, rather than the muon causing the trigger. This fraction was smaller than .0013 as will be shown below. The extra muons have a lower polarization P_μ due to cloud muon contamination (see section III.B), and a smaller average $\cos\theta_\mu$. When cloud muons are included, the average muon beam polarization is reduced to 99%. The mean $\cos\theta_\mu$ for the muon beam is 0.9966 compared to 0.9970 for muons which pass the $\cos\theta_\mu>0.99$ cut. Hence, a very small upward correction of $0.1\cdot10^{-4}$ could have been made to $\xi P_\mu\delta/\rho$ due to a smaller mean $\cos\theta_\mu$ and lower P_μ for extra muons. Since the correction was so tiny we have chosen

to ignore it.

Let us now compute the probability for an event to have the decay positron produced by an extra muon in the stopping target, rather than the muon causing the trigger. The muon causing the trigger will be referred to as the primary muon.

An extra muon may arrive either before or after the primary muon. First, consider extra muons arriving before the primary muon. Recall that the trigger consisted of two parts: a muon part, requiring a signature of a particle stopping in the target, followed in delayed coincidence of 0.1-10 μs by a positron part, requiring a particle registered by detectors downstream of the target. Let us denote by p_t the probability that an arriving muon will satisfy the requirement for the muon part of the trigger in the absence of deadtime. The probability p_t is estimated to be greater than 90%. Let λ denote the μ^+ beam rate. It can be shown that to a very good approximation for $\lambda\tau_\mu \ll 1$ the probability that there was another muon in the target when the primary muon had arrived is given by

$$(1-p_t)\lambda\tau_\mu + p_t\lambda^2\tau_\mu^2$$

where τ_μ is muon lifetime. The second term in the expression above is due to muons arriving in the 10 μs deadtime after each registered muon stop. For the average muon flux of 15 kHz, the probability that there was another muon in the target when the primary muon had arrived is therefore at the most 0.0043.

Consider now extra muons arriving after the primary muon. If an extra particle was detected upstream of the target after the primary muon had stopped, the event was cut in analysis if the 'extra-after'

particle was detected before the decay positron. The efficiency for detection of extra muons is estimated to be close to 100%, except for those arriving in the 300 ns notch after the primary muon. The notch, in which the extra particles were not detected, was necessary because of the after-pulsing in the proportional chambers P1 and P2, which resulted in false extra-after signals. For the average 15 kHz muon flux the probability of an extra muon arriving after the primary muon in the 300 ns notch is 0.0045.

If the decay positron was produced by an extra muon, there is only a 15% chance that such event will pass the cut requiring an agreement in track extrapolation at the stopping target. Therefore, the probability that the decay positron was produced by an extra muon (which arrived either before or after the primary muon) is at the most 0.0013, as mentioned above.

VIII. DISCUSSION AND CONCLUSIONS

VIII.A. Limit on $\xi P_\mu \delta/\rho$

We quote our result as a lower limit for $\xi P_\mu \delta/\rho$ since we are unable to correct for all possible sources of muon depolarization in the stopping target. Because our goal was to set a lower limit, we did not apply the possible upward corrections to $\xi P_\mu \delta/\rho$ discussed in sections V.D, VII.A and VII.B. In the absence of these corrections the combined result from all stopping targets

$$\xi P_\mu \delta/\rho = 0.99863 \pm 0.00046(\text{stat.}) \pm 0.00075(\text{syst.})$$

is still consistent (1.6σ) with the V-A prediction of 1. With the unphysical region ($\xi P_\mu \delta/\rho > 1$) excluded it implies the 90% confidence limit

$$\xi P_\mu \delta/\rho > 0.99747 \ .$$

The result is in agreement with the 90% confidence limit

$$\xi P_\mu \delta/\rho > 0.9951$$

obtained in the analysis of the spin-precessed data using the muon spin rotation (μSR) technique.[11,12] The combined result from the two methods of analysis implies the 90% confidence limit

$$\xi P_\mu \delta/\rho > 0.99753 \ .$$

The two methods of analysis have different major sources of possible systematic error, and it is therefore appropriate to combine the two results as independent measurements. The limit from the two results will be used to draw conclusions below.

So far it has been assumed that both left-handed and right-handed

neutrinos ν_μ and ν_e are massless or sufficiently light not to affect the kinematics (m_ν<1 MeV/c^2). We will continue to work in this limit until section VIII.G, where larger masses will be considered.

VIII.B. Limits on Right-Handed Currents with Massless Neutrinos

In the model with 'manifest' left-right symmetry (see section I) and massless neutrinos

$$\xi P_\mu \delta/\rho = 1-2(2\varepsilon^2+2\varepsilon\zeta+\zeta^2)$$

to lowest order in the mass-squared ratio ε and the mixing angle ζ for the gauge bosons W_1 and W_2. The lower limit on $\xi P_\mu \delta/\rho$ therefore constrains both ε and ζ. The contour corresponding to the 90% confidence limit on ε and ζ is plotted in Fig. I.1. Assuming $m(W_1)$=81 GeV/c^2, 90% confidence limits for the following special cases are obtained: $m(W_2)$>514 GeV/c^2 for ζ=0 and $m(W_2)$>432 GeV/c^2 when ζ is unconstrained; $|\zeta|$<0.035 for $m(W_2)=\infty$ and $-0.050<\zeta<0.035$ when $m(W_2)$ is unconstrained.

Herczeg[33] has obtained the expression for $(1-\xi P_\mu \delta/\rho)$ for a general left-right symmetric (LRS) theory, assuming that neutrinos are either sufficiently light that their effect on the spectrum can be ignored, or that they are too heavy to be produced in muon decay. In addition to ε and ζ, the general expression, which we do not reproduce here, contains the left-handed and right-handed weak coupling constants, the left-handed and right-handed quark mixing angles, the CP-violating phase in W_1 and W_2 mixing, and the mixing angles and CP-violating phases for neutrinos. For a general LRS

theory, constraints that are obtained from the limit on $\xi P_\mu \delta/\rho$ depend on the assumptions one makes about the values of these parameters.

VIII.C. Limits on $m(\nu_{\mu L})$ and $\nu_{\mu L}$ Helicity in π^+ Decay

The limit on $\xi P_\mu \delta/\rho$ implies limits on the mass of the left-handed muon neutrino and its helicity in pion decay. The weakest limits are obtained if it is assumed that right-handed currents are absent. In that case $\xi\delta/\rho=1$ and hence $P_\mu>0.9975$. The 90% confidence limit on the $\nu_{\mu L}$ helicity in π^+ decay is therefore $h(\nu_{\mu L})<-0.9975$. The corresponding limit on the $\nu_{\mu L}$ velocity ($\beta=v/c>0.9975$) in π^+ decay implies the 90% confidence limit $m(\nu_{\mu L})<2.1$ MeV/c^2. For comparison the world average value[21] $m(\nu_{\mu L})<0.5$ MeV/c^2 implies $P_\mu>0.99986$ in the absence of right-handed currents.

VIII.D. Restrictions on the Lorentz Structure of Leptonic Charged Weak Interactions

Mursula and Scheck[2] have recently obtained limits on non-(V-A) weak couplings using a helicity projection form of the flavor retention contact interaction Hamiltonian:

$$\begin{aligned} H = (G_0/\sqrt{2})\{&h_{11}(s+p)_{e\nu_e}(s+p)_{\nu_\mu\mu} + h_{12}(s+p)(s-p) + h_{21}(s-p)(s+p) \\ &+ h_{22}(s-p)(s-p) + g_{11}(v^\alpha+a^\alpha)(v_\alpha+a_\alpha) + g_{12}(v^\alpha+a^\alpha)(v_\alpha-a_\alpha) \\ &+ g_{21}(v^\alpha-a^\alpha)(v_\alpha+a_\alpha) + g_{22}(v^\alpha-a^\alpha)(v_\alpha-a_\alpha) \qquad (8.1) \\ &+ f_{11}(t^{\alpha\beta}+t'^{\alpha\beta})(t_{\alpha\beta}+t'_{\alpha\beta}) + f_{22}(t^{\alpha\beta}-t'^{\alpha\beta})(t_{\alpha\beta}-t'_{\alpha\beta})+\text{h.c.}\} \end{aligned}$$

where $s_{ik} = \overline{\psi}_i 1 \psi_k$, $p_{ik} = \overline{\psi}_i \gamma_5 \psi_k$, $v^{\alpha}_{ik} = \overline{\psi}_i \gamma^{\alpha} \psi_k$, $a^{\alpha}_{ik} = \overline{\psi}_i \gamma^{\alpha} \gamma_5 \psi_k$, $t^{\alpha\beta}_{ik} = \overline{\psi}_i (\sigma^{\alpha\beta}/\sqrt{2}) \psi_k$, $t'^{\alpha\beta}_{ik} = \overline{\psi}_i (\sigma^{\alpha\beta} \gamma_5/\sqrt{2}) \psi_k$ and the particle indices are as indicated in the h_{11} term.

There are several advantages to using a Hamiltonian of this form. For a pure (V-A) interaction only g_{22} is non-zero ($g_{22}=1$) while all other coupling constants vanish. Also, in the limit of massless particles the combinations of covariants in each term of equation (8.1) project onto states of definite helicity. As a consequence, the number of interference terms in any decay rate is minimal since only scalar-pseudoscalar and tensor terms interfere.

Several constraints are imposed on coupling constants in the models[2] with 'factorization and universality', where it is assumed that: (i) the charged weak interactions are mediated by a single heavy boson with spin 0, 1, or 2, (ii) V, A, T couplings are e-μ universal, but (iii) scalar and pseudoscalar coupling constants can be proportional to the charged lepton mass:

$$\begin{aligned} &h_{12},\ h_{21} \text{ real, positive semi-definite} \\ &h_{22}=h_{11}^{*} \text{ with } |h_{11}|^2=h_{12}h_{21} \\ &g_{11},\ g_{22} \text{ real, positive semi-definite} \\ &g_{21}=g_{12}^{*} \text{ with } |g_{12}|^2=g_{11}g_{22} \\ &f_{22}=f_{11}^{*}. \end{aligned} \tag{8.2}$$

In terms of the coupling constants in equation (8.1) the deviation of $\xi\delta/\rho$ from the V-A value of 1 is given by

$$1 - \xi\delta/\rho = \frac{8|g_{11}|^2+2|h_{21}|^2+2|h_{11}-2f_{11}|^2}{4(|g_{11}|^2+|g_{22}|^2)+|h_{12}|^2+|h_{21}|^2+|h_{11}-2f_{11}|^2+|h_{22}-2f_{22}|^2}$$

Hence the measurement of $\xi P_\mu \delta/\rho$ sets limits on g_{11}, h_{11}, h_{21}, and f_{11}. The weakest limits are obtained if it is assumed that the couplings responsible for μ^+ decay are unrelated to π^+ decay couplings. In this case the value of P_μ cannot be expressed in terms of the couplings in (8.1), and hence the limits are obtained from $\xi\delta/\rho \leq \xi P_\mu \delta/\rho$. If only one coupling other than the V-A coupling $g_{22}=1$ is non-zero the 90% confidence limit $\xi\delta/\rho>0.9975$ restricts $|g_{11}|$ or $|f_{11}|<0.035$ and $|h_{11}|$ or $|h_{21}|<0.070$. Stronger limits on the couplings can be obtained with assumptions of weak interaction universality. In the model with manifest left-right symmetry and no left-right mixing, for example, $P_\mu=1-2|g_{11}|^2/|g_{22}|^2$ to lowest order in g_{11}, and hence a 90% confidence limit on the V+A coupling g_{11} is $|g_{11}|<0.025$. The limits on g_{11}, f_{11}, h_{11}, and h_{21} in turn provide constraints on other couplings (e.g. f_{22}, h_{22}) in models with factorization and universality, which were discussed discussed in the paragraph above. These additional constraints are due to relations (8.2).

Although the limit on $\xi P_\mu \delta/\rho$ constrains the pure V+A coupling g_{11}, it does not constrain the couplings g_{12} and g_{21}, corresponding to the V-A coupling at one vertex ($e\nu_e$ or $\mu\nu_\mu$), but V+A coupling at the other vertex. The couplings g_{12} and g_{21} are constrained by the muon decay parameter ρ

$$\rho-3/4=-(12/A)\{|g_{12}|^2+|g_{21}|^2+2|f_{11}|^2+2|f_{22}|^2+\mathrm{Re}(h_{11}f_{11}{}^*+h_{22}f_{22}{}^*)\}$$

where

$$A = 4\{4(|g_{22}|^2+|g_{11}|^2+|g_{12}|^2+|g_{21}|^2)+|h_{11}|^2+|h_{12}|^2+|h_{21}|^2+|h_{22}|^2 + 12(|f_{11}|^2+|f_{22}|^2)\} .$$

Assuming that only g_{12} and g_{21} couplings are non-zero in addition to the V-A coupling $g_{22}=1$, the world average value[21] of $\rho=0.7517\pm0.0026$ implies the 90% confidence limit

$$\{|g_{12}|^2+|g_{21}|^2\}<0.0045$$

when the unphysical region $[(\rho-3/4)>0]$ is excluded.

VIII.E. Limits on Composite Leptons

The possibility that leptons and quarks are composite at some mass scale Λ has received considerable attention in recent years. Among the strongest experimental limits on Λ currently quoted[34] are those from the deviation of muon gyromagnetic ratio g from 2 (>860 GeV), ν-hadron scattering (>2.5 TeV), Bhabba scattering (1 to 3 TeV), and the reaction $e^+e^-\to\mu^+\mu^-$ (2-3.5 TeV).

The effects of compositeness may be analyzed in terms of new effective contact interactions. Following the analyses of Peskin,[35] and Lane and Barany[36] the most general SU(2)×U(1) invariant contact interaction contributing to $\mu \to e\nu\bar{\nu}$ is

$$\begin{aligned} L_{cont}=(g^2/\Lambda^2)[&\eta_1(\bar{\nu}_{\mu L}\,\gamma^\kappa\,\mu_L)(\bar{e}_L\,\gamma_\kappa\,\nu_{eL}) + \eta_2(\bar{\nu}_{\mu R}\,\gamma^\kappa\,\mu_R)(\bar{e}_R\,\gamma_\kappa\,\nu_{eR}) \\ &+ \eta_3(\bar{\nu}_{\mu L}\,\gamma^\kappa\,\nu_{eL})(\bar{e}_R\,\gamma_\kappa\,\mu_R) + \eta_4(\bar{e}_L\,\gamma^\kappa\,\mu_L)(\bar{\nu}_{\mu R}\,\gamma_\kappa\,\nu_{eR}) \\ &+ \eta_5(\bar{\nu}_{\mu L}\,\mu_R)(\bar{e}_L\,\nu_{eR}) + \eta_6(\bar{\nu}_{\mu L}\,\nu_{eR})(\bar{e}_L\,\mu_R) \\ &+ \eta_7(\bar{\nu}_{\mu R}\,\mu_L)(\bar{e}_R\,\nu_{eL}) + \eta_8(\bar{\nu}_{\mu R}\,\nu_{eL})(\bar{e}_R\,\mu_L)] \end{aligned} \tag{8.3}$$

where g is a coupling of hadronic strength; the η_i are usually assumed to be of order unity and are normalized so that $|\eta_L|=1$ in the diagonal coupling

$$(g^2/2\Lambda^2)[\eta_L(\bar{e}_L\gamma^\kappa e_L)(\bar{e}_L\gamma_\kappa e_L) + \ldots] .$$

The first and second terms in equation (8.3) are purely left-handed and right-handed respectively, and hence are indistinguishable from the usual V-A and V+A interactions.

There are three special cases of interest:

1. If only left-handed (right-handed) leptons are composite then only the purely left-handed (right-handed) term survives, i.e. only η_1 (η_2) $\neq 0$.
2. If both left-handed and right-handed leptons are composite but contain quite different sets of constituents then the purely left-handed and right-handed terms dominate, i.e. $\eta_1, \eta_2 >>$ other η_i.
3. If there is no ν_R, or $m(\nu_R)$ is large, only $\eta_1, \eta_3 \neq 0$.

Assuming an effective interaction Lagrangian $L_{eff} = L_{V-A} + L_{cont}$ we obtain the endpoint decay rate:

$$1 - \xi P_\mu \delta/\rho = 2(620\text{GeV}/\Lambda)^4 (g^2/4\pi)^2 (\eta_2^2 + \eta_3^2 + \eta_5^2/4) .$$

The limit $\xi P_\mu \delta/\rho > 0.9975$ then implies

$$\Lambda^2 > (3310\text{GeV})^2 (g^2/4\pi) \; (\eta_2^2 + \eta_3^2 + \eta_5^2/4)^{\frac{1}{2}}$$

with 90% confidence. (If the not unreasonable assumptions $g^2/4\pi \approx 2.1$ and $\eta_i > 0.2$ are made, the limit $\Lambda > 2600$ GeV would be obtained.)

For the special cases discussed earlier the limit becomes

1. Only left-handed leptons composite: no limit.

   Only right-handed leptons composite: $\Lambda^2 > (3310\text{GeV})^2 (g^2/4\pi)\eta_2$
2. Left- and right-handed leptons have different sets of constituents: $\Lambda^2 > (3310\text{GeV})^2 (g^2/4\pi)\eta_2$
3. No ν_R, or $M(\nu_R)$ large: $\Lambda^2 > (3310\text{GeV})^2 (g^2/4\pi)\eta_3$

VIII.F. Limits on Familons

It has been suggested by Wilczek[37] that the absence of large CP-invariance violations in strong interaction could be explained by a group of genuine flavor symmetries of the Lagrangian. Spontaneous breakdown of family symmetries leads to characteristic neutral massless Nambu-Goldstone bosons, which he called 'familons'. The coupling of familons at low energies is described by effective Lagrangians of the type

$$\Delta L = F^{-1}\, j_\lambda \partial^\lambda f$$

where F is the energy scale at which the flavor symmetry is spontaneously broken and j_λ is the appropriate current. Arguments based on cosmology suggest that $10^9 < F \leq 10^{12}$ GeV.

Familons may be detected by observing rare decay modes, in particular muon decay $\mu^+ \to e^+ + f$ with the branching ratio given by

$$b_{ef} = \frac{\Gamma(\mu \to ef)}{\Gamma(\mu \to e\nu\bar{\nu})} = \frac{2.5 \cdot 10^{14}\ \mathrm{GeV}^2}{F_{\mu e}^2}\ . \tag{8.4}$$

Since the decay $\mu \to ef$ is isotropic and familon is massless, the existence of familons would be indicated by a spike at the endpoint in the spin-held data (see Fig. V.1). The absence of such a spike allows us to obtain a limit on the branching ratio b_{ef} (8.4) and accordingly on the energy scale $F_{\mu e}$ at which the flavor symmetry is broken.

The fitting procedure for the computation of the branching ratio b_{ef} was essentially identical to that described in section V.A. Let us just mention that the decay rate $\mu \to ef$ was added to the fitting

function (5.3) for the spin-held data, and that this rate could be neglected in the fitting function for the spin-precessed data. The mean branching ratio, averaged over the five $\cos\theta_e$ bins and all stopping targets was found to be $(0.3\pm1.1)\cdot10^{-6}$. The systematic effects discussed in section VII contribute a possible systematic error of $\pm0.9\cdot10^{-6}$. The largest contribution ($\pm0.8\cdot10^{-6}$) is due to a possible difference in x=1 calibration between the spin-held and spin-precessed data sets. If the unphysical region ($b_{ef}<0$) is ignored 90% confidence limits

$$b_{ef}<2.6\cdot10^{-6}$$

and

$$F_{\mu e}>9.9\cdot10^{9}\ \text{GeV}$$

are obtained.

VIII.G. Limits on $m(W_2)$ with $m(\nu_{\mu R})\neq0$

It was mentioned in section I that if neutrinos are Majorana particles the left-handed and right-handed neutrinos may have different masses. So far only massless or very light neutrinos have been considered. In the most general case the limit on $m(W_2)$ that can be extracted from the data depends on the masses of the right-handed neutrinos, on neutrino mixing angles, and on the mixing angle ζ for W_1 and W_2. Here we present approximate limits on $m(W_2)$ for a particular case of massive Majorana neutrinos: we will assume a massive $\nu_{\mu R}$ with $m(\nu_{\mu R})\leq16.5$ MeV/c^2, and a very light ν_{eR}, $m(\nu_{eR})<1$ MeV/c^2. Manifest left-right symmetry will be assumed just

as before. For simplicity we will also assume that there is no mixing between W_1 and W_2, i.e. $\zeta=0$ and $W_2 \equiv W_R$, and that there is no mixing between neutrinos. The analysis method used in the computation of the limits is described in Appendix C. The limits on $m(W_2)$ are only approximate because of the lack of radiative corrections for the spectrum with massive neutrinos (they have not been computed), and also because of several simplifications in the treatment of systematic errors. The limits on $m(W_2)$ are expected to be accurate to ~2%.

The approximate limits on $m(W_2)$ versus $m(\nu_{\mu R})$, computed assuming $m(W_1)=81$ GeV/c^2, are shown in Fig. VIII.1. The allowed region is above the contour. It can be seen from Fig. VIII.1 that the limits on $m(W_2)$ are essentially the same for $m(\nu_{\mu R}) \leq 1$ MeV/c^2, but begin to drop rapidly below that value for $m(\nu_{\mu R}) > 6$ MeV/c^2. The valley at $m(\nu_{\mu R})=9$ MeV/c^2 corresponds to a 2.5σ deviation of $m(W_2)$ from ∞. For $m(\nu_{\mu R}) \geq 17$ MeV/c^2 the limits on $m(W_2)$ decrease dramatically since the endpoint of the V+A spectrum spectrum with a massive $\nu_{\mu R}$ approaches the minimum x=0.97 used in the fit of the spin-held data. The small discrepancy between the limit for $m(\nu_{\mu R})=0$ in Fig. VIII.1 and the value quoted earlier in section VIII.B is partly due to a different treatment of the systematic errors, and partly due to a small difference (0.0002) in the results from fitting of all the data in one $\cos\theta_e$ bin and from fitting the data separately for each target in five $\cos\theta_e$ bins.

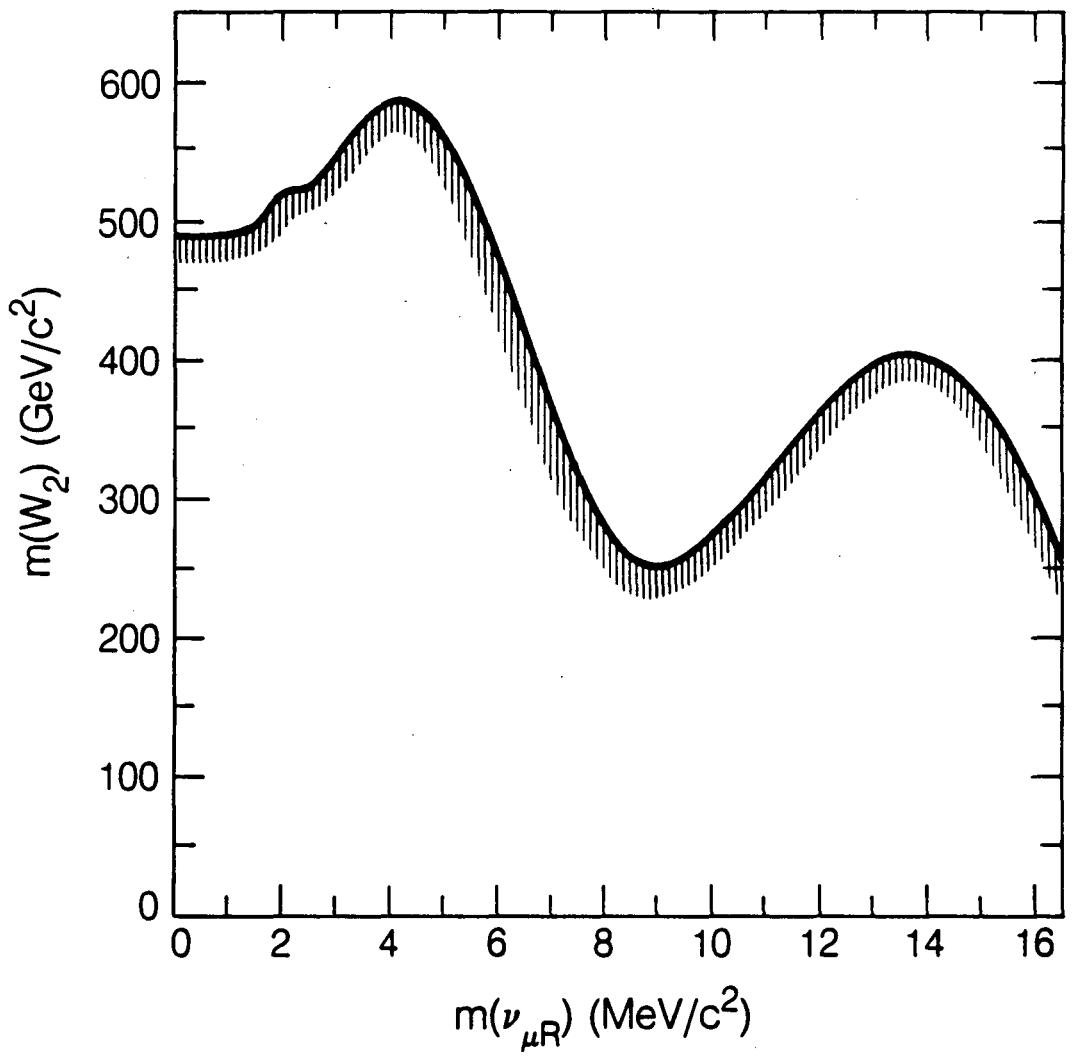

XBL 8512-11761

FIG. VIII.1. Approximate limits on $m(W_2)$ versus $m(\nu_{\mu R})$ assuming $m(\nu_{eR})<1$ Mev/c^2, no mixing for neutrinos and no mixing for the gauge bosons W_1 and W_2. The allowed region lies above the contour. The computation of the limits is described in the text.

VIII.H. Concluding Remarks

To summarize, we have made a precise measurement of the endpoint e^+ decay rate opposite to the μ^+ spin. The main conclusion is that the result of the measurement is consistent with the V-A model of weak interactions. We have used the result to deduce limits on the mass of the predominantly right-handed boson W_2 and the left-right mixing angle ζ in the left-right symmetric models; the $\nu_{\mu L}$ mass and helicity in π^+ decay; non-(V-A) couplings in helicity projection form; the mass scale of composite leptons; and the branching ratio for $\mu \to e+f$, where f (familon) is the neutral massless Nambu-Goldstone boson associated with flavor symmetry breaking.

Let us briefly consider the reduction in the error on $\xi P_\mu \delta/\rho$ that would be necessary to improve the limit on $m(W_2)$ by a factor of ~2. Assuming a central value of $\xi P_\mu \delta/\rho=1$, the 90% confidence limit $m(W_2)>800$ GeV/c^2 (with the left-right mixing angle ζ unconstrained) would require a combined statistical and systematic 1σ error of $\pm 1.1 \cdot 10^{-4}$. In view of several sources of possible systematic errors $>10^{-4}$, which were discussed in sections VI.A and VII, such accuracy would be very difficult to achieve with our experimental method.

In the absence of novel experimental techniques, the discovery of W_2, assuming that its mass is in the TeV region, will have to await the advent of high energy supercolliders. Eichten et al.[38] have considered the prospects for a discovery of W_2, or of an associated neutral gauge boson Z_2, at pp or $p\bar{p}$ machines. As a discovery criterion they have adopted the requirement that 1000 gauge bosons

are produced in the rapidity interval $|y|<1.5$. It was assumed that W_2 and Z_2 have similar branching ratios for leptonic decay and the same gauge couplings as W_1 and Z_1. For a $p\bar{p}$ collider with a center of mass energy of 40 TeV, for example, the maximum W_2 masses of 2.4, 4.7 and 8.0 TeV/c^2 were obtained for integrated luminosities of 10^{38}, 10^{39} and 10^{40} cm^{-2}. For the same luminosities the maximum Z_2 masses are 1.9, 3.8 and 7.1 TeV/c^2. The conclusion for the present moment, however, is that all experimental results are consistent with a standard $SU(2)_L \times U(1)$ electroweak model.

APPENDIX A: STOPPING TARGETS

The muons were stopped in high-purity (≥99.99%) metal foils or in liquid He. Since foils of optimum thickness were unavailable, the stopping targets were made either of two back-to-back foils, or of a single foil preceded and followed by 1 mil aluminum foils.

The stopping target thicknesses are tabulated in Table A.1. The compositions of targets having 1 mil Al foils are listed in upstream to downstream order. The mean amount of target material encountered by decay positrons is listed as 'residual thickness'. The residual thickness is also tabulated in terms of calculated μ^+ rms range straggling lengths. The effect of the 1% $\Delta p/p$ momentum bite has been included. Comparison of the calculated ranges with an experimental range curve taken in Run 2 (i.e. the second data-taking run) indicates that the error on the number of the residual straggling lengths is unlikely to exceed ±0.5.

The Ag and He targets were used only in Run 1. The residual thicknesses and straggling lengths for the other targets apply only to Run 2. For Runs 1 and 3 the residual thicknesses for Al, Au and Cu varied by small amounts from the Run 2 values due to use of magic gas (30% isobutane, 69.7% argon, 0.3% freon) in proportional chambers for Run 2 and the presence of an additional proportional chamber upstream of the target in Run 3. Let us mention here another minor difference between Runs 1, 2, and 3. During Run 1 the solenoid bore was filled with methane-8% methylal gas; during Run 2 a He bag was placed in the region between the driftchambers D2 and D3 (see

Fig. III.1); during Run 3 the He bag was removed and the solenoid bore was exposed to air.

TABLE A.1. The composition and thickness of the muon stopping targets. Superscript '*' denotes thicker targets.

Target	Run	Thickness (mg/cm^2)	Residual Thickness (mg/cm^2)	Residual Straggling Lengths
Ag	1	2× 136.5 Total 273	96	8.1
Al	1,2,3	150	35	4.6
Al*	2	2× 142.5 Total 285	171	22.6
Au	1,2	6× 6.6 Al 193 Au 6.6 Al Total 239	53 Au 6.6 Al Total 60	4.1
Cu	2	6× 6.6 Al 110 Cu 6.6 Al Total 156	16 Cu 6.6 Al Total 23	2.5
Cu*	1,2	2× 111 Total 222	81	8.3
He	1	38 Al 150 He 38 He Total 226	86 He 38 Al Total 124	17.2

APPENDIX B: TABLE OF DATA FITTING RESULTS

The results for $\xi P_\mu \delta/\rho$ are tabulated in Table B.1 for each target in the three data-taking runs, denoted by Run 1, etc.. Only statistical errors are shown. The systematic errors are discussed in sections VI and VII. The results incorporate the four corrections discussed in section VI. Table B.1 also lists the values of the target-dependent multiple Coulomb scattering correction to $\cos\theta_{av}$, discussed in section VI.A. Adding a correction to $\cos\theta_{av}$ is equivalent to reducing $\xi P_\mu \delta/\rho$ by the same amount. Target thicknesses have been compiled in Appendix A. The thicker targets are denoted by a superscript *.

TABLE B.1. Results for $\xi P_\mu \delta/\rho$ for each target in the three data-taking runs denoted by Run 1, etc.. Only statistical errors are shown. The last column lists the target-dependent Coulomb scattering correction discussed in section VI.A.

Run	Target	$\xi P_\mu \delta/\rho$	Scattering Correction to $\cos\theta_{av}$
1	Ag	$0.9983^{+0.0022}_{-0.0023}$	-0.0007
1	Al	$0.9972^{+0.0019}_{-0.0020}$	-0.0001
1	Au	$0.9956^{+0.0027}_{-0.0028}$	-0.0004
1	Cu*	$1.0014^{+0.0021}_{-0.0021}$	-0.0004
1	He	$0.9979^{+0.0022}_{-0.0023}$	-0.0001
2	Al	$0.9979^{+0.0011}_{-0.0011}$	-0.0001
2	Al*	$0.9995^{+0.0019}_{-0.0019}$	-0.0004

Table B.1 ...

Run	Target	$\xi P_\mu \delta/\rho$	Scattering Correction to $\cos\theta_{av}$
2	Au	$0.9993^{+0.0013}_{-0.0013}$	-0.0005
2	Cu	$0.9948^{+0.0013}_{-0.0013}$	-0.0001
2	Cu*	$1.0000^{+0.0021}_{-0.0021}$	-0.0004
3	Al	$0.9988^{+0.0012}_{-0.0012}$	-0.0001
3	Al#	$0.9985^{+0.0009}_{-0.0009}$	+0.0002

# denotes that the data was taken with 0.3-T longitudinal field rather than 1.1-T

Table B.1 (cont.)

APPENDIX C: COMPUTATION OF LIMITS ON $m(W_2)$ with $m(\nu_{\mu R})\neq 0$

We describe the analysis method used in the computation of limits on $m(W_2)$ as a function of $m(\nu_{\mu R})$ for $m(\nu_{\mu R})\leq 16.5$ MeV/c^2. We assume that ν_{eR} is very light, $m(\nu_{eR})<1$ MeV/c^2, that there is no mixing between W_1 and W_2, i.e. $\zeta=0$ and $W_2\equiv W_R$, and that there is no mixing between neutrinos.

The muon decay rate for massive neutrinos has been calculated by Shrock.[39] If radiative corrections, positron mass, and ν_{eR} mass are neglected, the V+A differential decay rate is given by

$$\frac{d^2\Gamma}{dx\,d(\cos\theta)} \sim (1-\nu^2/k^2)^2\, x^2\{(3-2x)+(3-x)\nu^2/k^2 - \cos\theta[1-2x-(1+x)\nu^2/k^2]\}$$

where $\nu=m(\nu_{\mu R})$, $k^2=m_\mu^2-2m_\mu E_e$, and $x\equiv E_e/E_0$. Here E_0 is the maximum positron energy for the spectrum with massless neutrinos (i.e. E_0 is equal to E_{max} in section II). The maximum positron energy for a spectrum with a massive $m(\nu_{\mu R})$ is $E_{max}=(m_\mu{}^2-\nu^2)/(2m_\mu)$.

Radiative corrections to the muon decay spectrum have been calculated only for the case of massless neutrinos. Hence, in fitting with massive neutrinos we used the V+A spectrum without radiative corrections, but made an adjustment (described below) to the fitted value for the V+A decay rate in order to compensate for the missing corrections. The limits on $m(W_2)$ that we have computed are therefore only approximate because of the lack of radiative corrections, and also because of several simplifications in the treatment of systematic errors. The limits on $m(W_2)$ are expected to be accurate to ~2%.

The V+A decay rate <u>without</u> the radiative corrections is plotted in Fig. C.1 for $\cos\theta=1$ and $m(\nu_{\mu R})=0$, 5, 10, 15 and 20 MeV/c^2 (solid curves). For comparison, the radiatively corrected V+A rate for $m(\nu_{\mu R})=0$ and $\cos\theta=1$ is shown by the dashed curve. The ratio of the radiatively corrected V+A rate to the uncorrected rate for $m(\nu_{\mu R})=0$ is nearly independent of $\cos\theta$ for $\cos\theta$ near 1. It decreases from 0.95 at x=0.97 to 0.93 at x=0.99 approximately linearly; above x=0.99 it decreases much more rapidly and approaches 0 as $x\to 1$.

If neutrinos are massive Majorana particles there are four distinct final states in muon decay (it is assumed that there is no neutrino mixing). If $\nu_{\mu R}$ is massive but ν_{eR} is very light, then the measured spectrum corresponding to the spin-held data will be proportional to the sum

$$S_{V-A}(x,P_\mu\cos\theta_{av}) + \varepsilon^2\, S_{V+A,\nu}(x,P_\mu\cos\theta_{av}) \tag{C1}$$

where $S_{V-A}(x,P_\mu\cos\theta_{av})$ denotes the V-A spectrum for muon polarization equal to P_μ and $\cos\theta=\cos\theta_{av}$, ε is the mass-squared ratio for the gauge bosons W_1 and W_2, and $S_{V+A,\nu}(x,P_\mu\cos\theta_{av})$ is the V+A spectrum for a massive $\nu_{\mu R}$ with the same normalization as $S_{V-A}(x,P_\mu\cos\theta_{av})$.

Recall that in the case of massless neutrinos the fitting function for the spin-held data (V.3) was based on the equation (2.2). The sum (C1) can also be written in a form similar to the equation (2.2)

$$[1-r(\theta_{av})]S_{V-A}(x,1) + r(\theta_{av})S_{V-A}(x,0)$$
$$+ \varepsilon^2\{[1-r(\theta_{av})]S_{V+A,\nu}(x,1) + r(\theta_{av})S_{V+A,\nu}(x,0)\}$$

where

$$r(\theta_{av})=1-P_\mu\cos\theta_{av}\ .$$

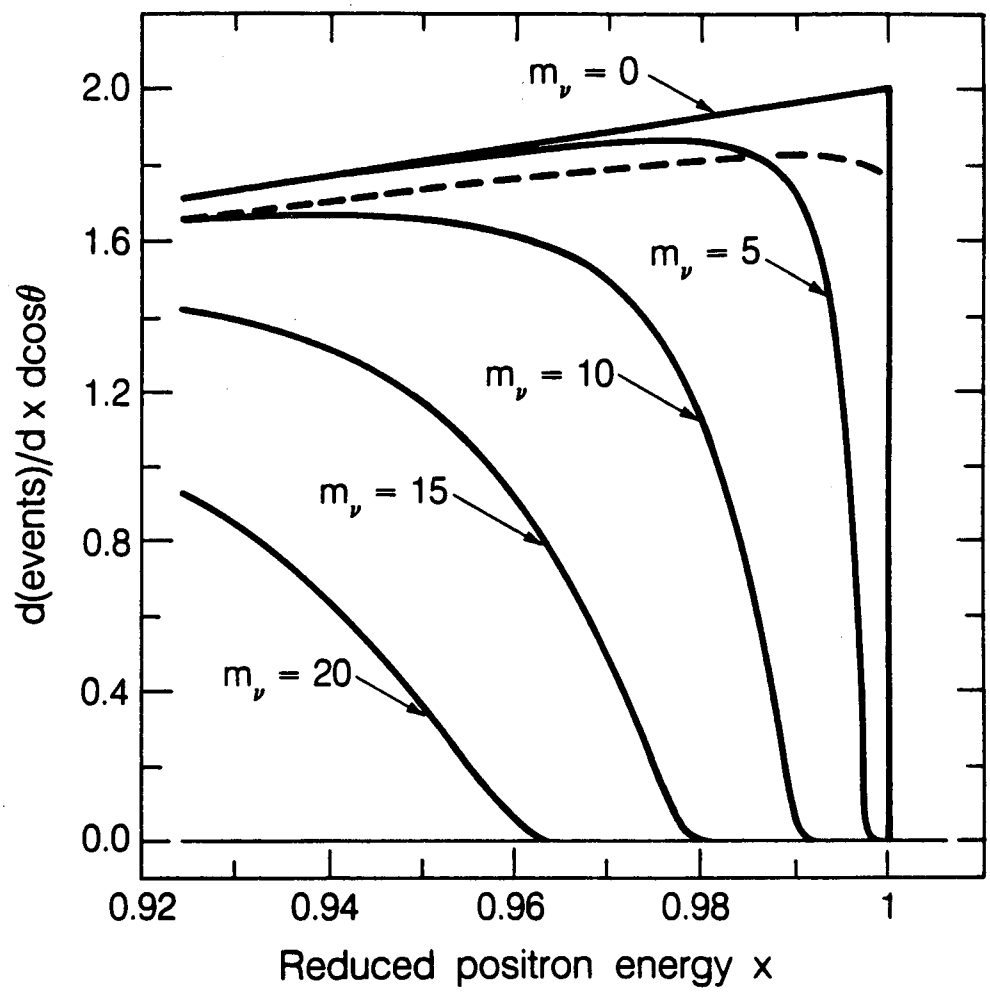

XBL 8512-11760

FIG. C.1. The V+A muon decay rate without radiative corrections for $m(\nu_\mu)$=0, 5, 10, 15, and 20 MeV/c^2 assuming massless ν_e (solid curves). The dashed curve is the V+A radiatively corrected decay rate for $m(\nu_\mu)=m(\nu_e)=0$. The decay rates are plotted for the reduced positron energy x>0.92. They are normalized so that the integral of the radiatively corrected rate is 1.

The fitting procedure for the case of massive neutrinos was therefore very similar to that for massless neutrinos described in section V.A and we will not describe it in detail. The primary difference was that in the fitting function for the spin-held data there was one more free parameter ε, which was constrained to be greater or equal to zero. For the fitting function for the spin-precessed data, it was determined that the contribution of $S_{V+A,\nu}(x,0)$ could be ignored because it changed the limit on $m(W_2)$ by less than 0.5%.

There was, however, an additional constraint on ε imposed by the fitted value of the relative rate at the endpoint $r(\theta_{av})$ (i.e. of $1-P_\mu\cos\theta_{av}$) since for a sufficiently light $\nu_{\mu R}$ the polarization of the muon beam delivered to the polarimeter would have been reduced by the effects of the same right-handed currents. The reduction in muon beam polarization due to possible right-handed currents is given by

$$\Delta P_\mu = 2\varepsilon^2\beta_\nu F(m_\nu) \tag{C2}$$

where β_ν is the velocity of $\nu_{\mu R}$ in π^+ decay at rest and $F(m_\nu)$ is the fraction of muons in the beam which were produced in π^+ decays mediated by W_2. The fitted value of $r(\theta_{av})$ was therefore constrained to be

$$r(\theta_{av}) \geq 1-(1-\Delta P_\mu)\cos\theta_{av}$$

with ΔP_μ given by (C2).

The fraction $F(m_\nu)$, defined just above, decreased as $m(\nu_{\mu R})$ increased and as the momentum of the muons, produced in π^+ decays mediated by W_2, approached the lower boundary of the beamline momentum bite. For simplicity this fraction was computed assuming a uniform distribution in the 1% beam momentum bite $\Delta p/p$. The mean

beam momentum was taken to be 29.45 MeV/c. $F(m_\nu)$ vanished for $m(\nu_{\mu R})>5$ MeV/c^2.

The limits on ε [which in turn determine the limits on $m(W_2)$] were computed for $m(\nu_{\mu R})$ varying from 0 to 16.5 MeV/c^2 in steps of 0.5 MeV/c^2. For $m(\nu_{\mu R})\geq 17$ MeV/c^2 the limits on ε increased dramatically since the endpoint of the spectrum $S_{V+A,\nu}(x,P_\mu\cos\theta_{av})$ approached the minimum x=0.97 used in the fit of the spin-held data. In order to reduce the computational effort only one fit was made for each value of $m(\nu_{\mu R})$. The fit was made to the data from all targets in one $\cos\theta_e$ bin ($\cos\theta_e\geq 0.975$). Furthermore, since the systematic error in ε was different for each value of $m(\nu_{\mu R})$, only the largest systematic errors were considered. For $m(\nu_{\mu R})>5$ MeV/c^2, when there was no constraint on ε from $r(\theta_{av})$ [$r(\theta_{av})=1-P_\mu\cos\theta_{av}$], the systematic error in $\cos\theta_{av}$ did not propagate into an error in ε. Hence, the largest systematic errors in ε for $m(\nu_{\mu R})>5$ MeV/c^2 were due to possible differences in x=1 calibration and x acceptance between the spin-held and spin-precessed data sets (see sections VII.A and VII.B). For simplicity, only these two errors were considered also for $m(\nu_{\mu R})$ less than 5 MeV/c^2.

In order to account for these systematic errors, the limis on ε were computed for the four different cases corresponding to $\Delta x_1=\pm 0.45\cdot 10^{-4}$ and $D_1=\pm 0.2$, where Δx_1 and D_1 are defined in sections VII.A and VII.B respectively. Of the four limits the most conservative limit on ε was chosen corresponding to the highest value. For each fit the upper limit on ε was taken to be the sum of the fitted value, constrained to be greater or equal to zero, plus a

positive error corresponding to an increase in χ^2 of 1.638. [$1.638=1.28^2$; the probability of an answer lying more than 1.28σ above a gaussian with a standard deviation σ is 10%.]

As mentioned above, the limits on ε were computed using the spectrum $S_{V+A,\nu}(x,P_\mu\cos\theta_{av})$ without the radiative corrections. For $m(\nu_{\mu R})=0$ the fitted value for ε was compared to the value found when the radiative corrections were included. Agreement in the two values could be obtained if the former were multiplied by 1.04. Since the effect of the radiative corrections is greatest near the endpoint, one would expect that the adjustment in the fitted value for ε should be smaller for $m(\nu_{\mu R})>0$, because the spectrum for $m(\nu_{\mu R})>0$ rises more slowly near the endpoint (see Fig. C.1). Conservatively, however, the limits on ε were multiplied by 1.04 for all values of $m(\nu_{\mu R})$.

The approximate limits on $m(W_2)$ versus $m(\nu_{\mu R})$, computed from the limits on ε assuming $m(W_1)=81$ GeV/c^2, are shown in Fig. VIII.1 in section VIII.F. These limits were commented upon in the last paragraph of that section.

REFERENCES

1 S. Glashow, Nucl. Phys. 22, 529 (1961); S. Weinberg, Phys. Rev. Lett. 19, 1264 (1967); A. Salam, in Elementary Particle Theory, ed. N. Svastholm (Stockholm, 1968)

2 K. Mursula, M. Roos, and F. Scheck, Nucl. Phys. B219, 321 (1983); K. Mursula and F. Scheck, Nucl. Phys. B253, 189 (1985).

3 J.C. Pati and A. Salam, Phys. Rev. D10, 275 (1974); R.N. Mohapatra and J.C. Pati, Phys. Rev. D11, 566, 2558 (1974); G. Senjanovic and R.N. Mohapatra, Phys. Rev. D12, 1502 (1975).

4 G. Senjanovic, Nucl. Phys. B135, 334 (1979).

5 M. Gell-Mann, P. Ramond, and R. Slansky (unpublished); R. N. Mohapatra and G. Senjanovic, Phys. Rev. D23, 165 (1981).

6 G. Beall, M. Bander, and A. Soni, Phys. Rev. Lett. 48, 848 (1982); R. N. Mohapatra, G. Senjanovic, and M. D. Tran, Phys. Rev. D28, 546 (1983); F.J. Gilman and M.H. Reno, Phys. Lett. 127B, 426 (1983).

7 J. Donahue and B. Holstein, Phys. Lett. 113B, 382 (1982). See also I.I. Bigi and J.M. Frere, Phys. Lett. 110B, 255 (1982).

8 F.I. Olness and M.E. Ebel, Phys. Rev. D30, 1034 (1984).

9 L. Wolfenstein, Phys. Rev. D29, 2130 (1984)

10 M.A.B. Beg, R.V. Budny, R. Mohapatra, and A. Sirlin, Phys. Rev. Lett. 48, 1252 (1977); B.R. Holstein and S.B. Treiman, Phys. Rev. D16, 2369 (1977).

11 D.P. Stoker, et al., Phys. Rev. Lett. 54, 1887 (1985).

12 D.P. Stoker, Ph. D. Thesis, LBL report LBL-20324 (1985).

[13] The primary input to the world average is V.V. Akhmanov, et al., Yad. Fiz. 6, 316 (1967)

[14] The primary input to the world average is J. Peoples, Nevis Cyclotron Report No. 147 (1966) (unpublished).

[15] J. Van Klinken, Nucl. Phys. 75, 145 (1966)

[16] J. Van Klinken, et al., Phys. Rev. Lett. 50, 94 (1983)

[17] D. Schreiber and F.T. Calaprice, private communication; D. Schreiber, Ph.D. Thesis, Princeton University, 1983 (unpublished). We calculated the contour plotted in Fig. I.1 using A(0)=.0363±.0008; ft ratio = 1.797±.002. See also F.T. Calaprice, S.J. Freedman, W.C. Mead, and H.C. Vantine, Phys. Rev. Lett. 35, 1566 (1975).

[18] H. Abramowicz, et al., Z. Phys. C12, 225 (1982).

[19] T.D. Lee and C.N. Yang, Phys. Rev. 108, 1611 (1957).

[20] F. Scheck, Phys. Lett. 44C, 187 (1978).

[21] C.G. Wohl, et al. (Particle Data Group), Rev. Mod. Phys. 56, S1 (1984). Primary input to ρ is Ref. 14; primary input to η is F. Corriveau et al., Phys. Lett. 129B, 260 (1983) and S.E. Derenzo, Phys. Rev. 181, 1854 (1969); primary input to ξP_μ is Ref. 13; primary input to δ is D. Fryberger, Phys. Rev. 166, 1379 (1968).

[22] Radiative corrections in muon decay are reviewed by A.M. Sachs and A. Sirlin, in Muon Physics, Vol. II, V. Hughes and C.S. Wu, eds. (Academic Press, New York, 1975).

[23] M.A.B. Beg and A. Sirlin, Ann. Rev. Nucl. Sci. 24, 579 (1974).

[24] V. Fluorescu and O. Kamei, Nuovo Cimento 61A, 967 (1968).

[25] A.E. Pifer, T. Bowen, and K.R. Kendall, Nucl. Inst. Meth. 135, 39 (1976).

[26] C.J. Oram, J.B. Warren, G.M. Marshall, and J. Doornbos, Nucl. Inst. Meth. 179, 95 (1981).

[27] The deceleration and thermalization of muons in matter has been reviewed by J.H. Brewer, K.M. Crowe, F.N. Gygax, and A. Schenck, in Muon Physics, Vol. III, V. Hughes and C.S. Wu, eds. (Academic Press, New York, 1975).

[28] G.W. Ford and C.J. Mullin, Phys. Rev. 108, 477 (1957).

[29] V. Hughes, Phys. Rev. 108, 1106 (1957).

[30] R. Sagane, W. Dudziak, and J. Vedder, Phys. Rev. 95, 863 (1954).

[31] K. Halbach, private communication. The mathematical formalism of first-order optics approximation for cylindrically symmetric field is outlined in Appendix A of Ref. 12.

[32] B.P. Nigam, M.K. Sundaresan, and T.A. Wu, Phys. Rev. 115, 491 (1959); J.B. Marion and B.A. Zimmerman, Nucl. Instr. Meth. 51, 93 (1967).

[33] P. Herczeg, LANL preprint LA-UR-85-2761.

[34] M. Abolins et al., in Proc. 1982 DPF Summer Study on Elem. Part. Phys. and Future Facilities, p. 274, R. Donaldson, R. Gustafson, and F. Paige, eds. (Snowmass, 1982); S. Yamada, in Proc. XXII Int. Conf. on High Energy Physics, p. 72, A. Meyer and E. Wieczorek, eds. (Leipzig, 1984); M. Althoff, et al., Z. Phys. C22, 13 (1984).

[35] M.E. Peskin, private communication.

[36] K.D. Lane and E. Barany, private communication.

[37] F. Wilczek, Phys. Rev. Lett. 49, 1549 (1982).

[38] E. Eichten, I. Hinchliffe, K. Lane, and C. Quigg, Rev. Mod. Phys. 56, 579 (1984).

[39] R.E. Shrock, Phys. Rev. D24, 1275 (1981).

This report was done with support from the Department of Energy. Any conclusions or opinions expressed in this report represent solely those of the author(s) and not necessarily those of The Regents of the University of California, the Lawrence Berkeley Laboratory or the Department of Energy.

Reference to a company or product name does not imply approval or recommendation of the product by the University of California or the U.S. Department of Energy to the exclusion of others that may be suitable.

LAWRENCE BERKELEY LABORATORY
TECHNICAL INFORMATION DEPARTMENT
UNIVERSITY OF CALIFORNIA
BERKELEY, CALIFORNIA 94720